Influence of Embedded Metallic Nanocrystals on GaAs Thermoelectric Properties

by

Michael V. Warren

A dissertation submitted in partial fulfillment
of the requirements for the degree of
Doctor of Philosophy
(Materials Science and Engineering)
in the University of Michigan
2014

Doctoral Committee:

Professor Rachel S. Goldman, Chair
Professor Roy Clarke
Assistant Professor Emmanouil Kioupakis
Professor Ctirad Uher

Acknowledgments

I would like to thank my fiancée Kathryn, friends, and my family. I would also like to thank my advisor, Rachel S. Goldman, and my committee members Roy Clarke, Emmanouil Kioupakis, and Ctirad Uher for their helpful discussions, guidance, and support. Special thanks go to my fellow group members, past and present.

Support from the U.S. Department of Energy through the Center for Solar and Thermal Energy Conversion, an Energy Frontier Research Center, under Award Number DE-SC0000957 is gratefully acknowledged. This work was also supported in part by the GAANN Fellowship

Table of Contents

List of Figures

List of Tables

List of Appendices

Abstract

Influence of Embedded Metallic Nanocrystals on GaAs Thermoelectric Properties

by

Michael V. Warren

Chair: Rachel S. Goldman

For the past several years, there has been significant interest in low-dimensional structures, such as superlattices, nanocrystals, and nanowires, for thermoelectric applications due to their ability to enhance the figure-of-merit. These nanostructured materials must be optimized to maximize the Seebeck coefficient (S) and electrical conductivity (σ) while minimizing the thermal conductivity (κ). Due to the possibility of nucleating nanocrystals within an amorphous matrix, ion-beam-synthesized nanocomposites show promise as possible thermoelectric materials. To optimize these ion-beam-synthesized nanocomposites, an understanding of the microstructure and thermoelectric properties is essential. Here, we report on the formation of metallic In (Bi) nanocrystals (NCs) embedded in GaAs by In (Bi) ion implantation and rapid thermal annealing (RTA). The role of microstructure on the thermoelectric properties of ion-implanted GaAs is discussed via a comparison of GaAs:Bi, GaAs:In and GaAs:N films.

We report on the relationship between microstructure and thermoelectric properties of ion-beam-synthesized In NCs in GaAs. We developed a sputter-mask method to enhance the retained ion dose. During annealing, In NCs are nucleated within a polycrystalline GaAs matrix. Electrons and phonons are scattered at interfaces, reducing σ, κ, and consequently the thermoelectric efficiency in comparison to that of unimplanted GaAs.

We also report on the formation of Bi NCs embedded in GaAs and their influence on the thermoelectric properties. Implantation-induced defects reduce the free carrier concentration, n, and, consequently, σ, while annealing results in a partial recovery of n and σ. Phonon scattering at Bi NC boundaries serves to reduce κ by ~30% for all films. We discuss the role of microstructure on the electrical and thermal conductivity of the GaAs:Bi films through a comparison with GaAs:In and GaAs:N films, demonstrating a general trend of n and σ reduction following ion-implantation, while a partial recovery of n and σ, and a reduction in κ due to phonon scattering, follows RTA.

This thesis reveals new insights into the structure-property relationship of ion-implanted GaAs. Embedded metallic NCs show promise for thermoelectric applications via κ reduction. Based on these results, it is suggested that epitaxial growth of embedded NCs will result in a reduction in κ while simultaneously preserving σ.

Chapter 1

Introduction

1.1 Overview

In the past few years, alternative means of energy production and energy conservation have become increasingly important international concerns. Thermoelectric devices, which directly convert heat to electricity, are one possible method of addressing these concerns. The low efficiency of current thermoelectric materials, however, has prevented the widespread implementation of thermoelectric devices. Over the past 20 years, nanostructuring has been investigated as a method for increasing the efficiency of thermoelectric materials.[1] These nanostructures include quantum wells,[2] nanometer-scale polycrystalline materials,[3] 3-dimensional modulation doping,[4] and semimetallic[5] and metallic nanocrystals embedded within a semiconductor.[6]

This chapter opens with the motivation for studies of nanostructured semiconductor materials for thermoelectric applications. Next, we review the growth methods of semiconductor nanostructures. Finally, the chapter concludes with an outline and objectives of the dissertation.

1.2 Thermoelectric Devices

In 1823, Thomas Johann Seebeck reported the movement of a compass needle when placed within a loop of two conductors and one junction was heated.[7] Though he was unaware of it at the time, this experiment demonstrated the conversion of heat to electrical energy; a conversion now called the "Seebeck effect." The applications of the Seebeck effect for power generation, however, started being investigated in the 1950's.[8] At this time, the design of a modern thermoelectric device was standardized. This design consists of two electrically insulating, thermally conducting ceramic plates, between which is a series of alternating *n*- and *p*-type semiconductor legs. These semiconductor legs are arranged so that they are parallel to the temperature gradient, while being connected electrically in series. A schematic of such a structure is shown in Fig. 1.1. By arranging the semiconductor legs parallel to the temperature gradient, electrons and holes will move from the hot to the cold end of the *n*- and *p*-type semiconductors, respectively.[9] Because these semiconductors are connected in series electrically, the electrical power generated by each leg is added, allowing for a higher power output in comparison to a single thermocouple.[7]

This design of a thermoelectric device provides certain advantages over mechanical power generation methods. Due to an absence of moving parts and reliable design, thermoelectric devices have seen use as power generators in outer planet space missions, such as Voyagers 1 and 2 and the Cassini missions.[10] Indeed, the thermoelectric generators powering the Voyager probes have been operating for 36 years. The compact size of thermoelectric generators has also prompted the study of their implementation for

waste heat recovery in automotive applications. It is estimated that only 25% of the energy liberated during fuel combustion is utilized for motion, while 40% of the energy is wasted as exhaust heat.[10] It is proposed that using a thermoelectric generator to convert a portion of this exhaust heat to electricity could reduce engine loads and increase fuel efficiency. Finally, as more focus is placed upon utilizing environmentally friendly means of electrical energy production, thermoelectric generators have been a point of interest for converting waste heat to electricity.[7] In most cases, however, thermoelectric generators have not seen widespread adoption due to their low efficiency (the exception being space-based applications where weight is a higher priority than efficiency).

1.3 Thermoelectric Properties

Low-dimensional structures are predicted to lead to an increased thermoelectric figure-of-merit, *ZT*, in comparison to bulk materials. *ZT* is defined as:

$$ZT = \frac{S^2 \sigma}{\kappa} T \tag{1.1}$$

where σ is the electrical conductivity, S is the Seebeck coefficient, T is temperature, and κ is the thermal conductivity. In bulk materials, such as metals and non-degenerate semiconductors,[11] the electrical conductivity and electronic contribution to the thermal conductivity (κ_e) are related via the Wiedemann Franz law:

$$\frac{\kappa_e}{\sigma T} = C_{WFL} \tag{1.2}$$

where C_{WFL} is a constant (the Wiedemann-Franz-Lorenz coefficient). Therefore, an increase in σ yields a proportional increase in κ_e, resulting in a negligible net benefit in *ZT*. Studies of quantum confined structures have led to predictions[12] and observations[13] that the electrical and thermal conductivities may be decoupled. Additionally, phonon scattering at phase boundaries between nanoparticles and matrix is expected to lead to a decrease in thermal conductivity.[1,14] Additionally, due to the increased control of the density of states and hence, the energies of charge carriers, nanocomposite materials are predicted to have a significantly higher thermoelectric power factor ($S^2\sigma$) compared to bulk materials.[15] Nanoscale (~1.5 nm) inclusions of metallic and semimetallic particles are predicted to enhance the Seebeck coefficient via electron energy filtering.[16] For example, 2 – 3 nm sized ScErAs nanoparticles embedded in InGaAs have been shown to increase the thermoelectric figure of merit from 0.0045 to 0.13.[17] In addition, arrays of 10 nm diameter InAs quantum dots have been predicted to exhibit an increased thermoelectric power factor in comparison with bulk GaAs. [18,19]

Multi-component nanostructured thermoelectrics such as $Bi_2Te_3/Sb_2/Te_3$ thin-film superlattices have resulted in several improvements in ZT.[2] By varying the size and impurity levels in nanostructured Si, 100-fold improvements in ZT over bulk Si have been reported.[20] These developments are expected to be extrapolated to other classes of semiconductor nanomaterials, with several recent advances in the development of these materials for thermoelectric applications. For example, nanostructured porous GaAs has been reported to exhibit a thermal conductivity decreasing with particle size, resulting in an order of magnitude decrease in thermal conductivity compared to bulk GaAs.[21] Additionally, nanostructured GaAs is predicted to exhibit a thermoelectric power factor

450% larger in comparison to its bulk counterpart.[22] In both cases, the thermoelectric properties are heavily dependent on the nanostructure size.

1.4 Synthesis of Nanostructures

Several techniques have been explored for the synthesis of nanostructured thermoelectric materials including ball milling, epitaxial methods, and ion-beam synthesis. In this section, we review these various growth methods and their ability to control nanostructure size and composition.

1.4.1 Ball Milling

One method of synthesizing nanostructures relevant to thermoelectric applications is ball milling. Ball milling produces powders which, following densification, have yielded materials with grains approximately 20 nm in diameter.[23] However, these materials can have a large variation in grain size, ranging from <10 nm to hundreds of nm.[24] The decomposition of these materials into grains of the constituent elements during densification has also been reported.

1.4.2 Epitaxy

Nanostructured thermoelectric materials have also been synthesized via epitaxial growth. In an effort to scatter phonons and therefore reduce the thermal conductivity, $Bi_2(Se_xTe_{1-x})_3$/ $Bi_2(Se_yTe_{1-y})_3$ and $PbTe/PbSe_xTe_{1-x}$ superlattices have been grown via molecular beam epitaxy (MBE).[25] Additionally, MBE has been used to fabricate superlattices of PbSe nanodots embedded in PbTe.[26] These nanodots grow in the Stanski-Krastanov mode, with deposition of a wetting layer of about two monolayers, followed by 3D islanding.[27] However, the size of these nanodots is a function of the lattice mismatch between nanodot and matrix, limiting the producible feature size.

Despite numerous methods for the formation of nanostructured thermoelectric materials, it is still a challenge to fabricate nanostructures with controlled size. Additionally, these structures can decompose into constituent elements during thermal processing, altering the chemistry and thermoelectric properties of the material. While MBE offers control over the composition of the nanostructures, these methods are limited by the inability to tune the size of the nanostructures.

1.4.3 Ion-Beam Synthesis

Due to the wide range of available implant and target species, as well as adjustable implantation ion doses and energies, ion implantation is becoming an increasingly popular technique for nanostructure synthesis.[28] Using ion implantation techniques, a target material is irradiated with energetic ions that are accelerated from tens to thousands of kilovolts. High-dose implantations can create a target supersaturated

with the implanted ions in a layer ranging from the specimen surface to depths up to hundreds of nanometers.[29] Subsequent thermal processing or further ion irradiation can induce the implanted material to precipitate as discrete nanoparticles.[30,31,32] However, it is necessary to note that implantation-induced damage can negatively alter the electrical and thermal transport properties.

Since essentially any element can be implanted into virtually any host material, ion implantation is extremely versatile. The large variety of ion/host permutations leads to a wide range of potential nanoparticle/host combinations, including SiO_2:Si and SiO_2:CdSe,[33] Si:Fe,[34] SiO_2:Ge,[35] Al_2O_3:CdS,[36] and GaAs:N.[37] Thus, a single well-defined and integrated structure could exhibit useful properties of two or more phases. By tuning the density and size of the precipitates, the properties of interest of the nanocomposite would be optimized. There are multiple approaches to tuning the size of precipitates, including adjusting the concentration of implanted ions (e.g., by varying the dose, ion current, and energy), and altering the annealing parameters.[28] However, to date, the implantation and annealing parameters required for specific precipitates are limited.

A promising approach to fabricating embedded nanostructures is matrix-seeded growth, which consists of ion-beam-amorphization of a semiconductor film, followed by annealing, shown schematically in Fig. 1.2.[37] High-energy ion implantation results in a supersaturated layer (Fig. 1.2(a)), and nanocrystallization in the matrix is induced via annealing (Fig. 1.2(b)). For example, nucleation of GaN nanocrystals within an amorphous matrix has been achieved using N-ion implantation into epitaxial-GaAs, followed by rapid-thermal-annealing (RTA).[38] In this thesis, we will present an extension of this technique to GaAs:In and GaAs:Bi

1.5 Dissertation Objectives

The first part of this thesis focuses on In nanocrystal formation in In^+ implanted GaAs. We first examine the influence of ion fluence and 600ºC RTA on the microstructure and thermoelectric properties of the films. At this annealing temperature, no In nanocrystals are observed. However, an ion fluence of $3.8x10^{16}$ cm^{-2} is identified as the fluence corresponding to maximum retained In concentration. We note that both the resistivity and Seebeck coefficient increase with increasing ion fluence, with an enormous Seebeck coefficient of -12 mV/K at 4 K for the highest fluence film. We then study the influence of annealing temperature on In^+ implanted GaAs. We show RTA at 450ºC leads to the nucleation of metallic In nanocrystals within a polycrystalline GaAs layer. These In nanocrystals act as electron donors, increasing the free carrier concentration in comparison to those films annealed at higher temperatures. The increase in interfacial density serves to scatter more phonons, decreasing the thermal conductivity by ~50% in comparison to bulk GaAs. We propose this work as a starting point for methods to improve ZT of GaAs.

The second portion of this thesis focuses on Bi nanocrystal formation in Bi^+ implanted GaAs. We study the effect of ion fluence on nanocrystal formation and their influence on thermoelectric properties. For all fluences, Bi nanocrystal formation within crystalline GaAs is observed, yet these nanocrystals have a negligible influence on the Seebeck coefficient. The thermal conductivity of all films is decreased by ~30%

presumably due to a combination of phonon scattering at nanocrystal boundaries and implantation-induced defects and phonon scattering due to the high mass mismatch between Bi and Ga and As.

1.6 Dissertation Organization

This dissertation is organized as follows. Chapter 2 describes the experimental procedures used for this thesis work, including sample growth, ion implantation, transmission electron microscopy (TEM), electrical transport measurements, and time-domain thermoreflectance (TDTR) measurements of the thermal conductivity. Details of TEM sample preparation are also presented.

In Chapter 3, the nucleation of In nanocrystals in GaAs is described. The first portion of the chapter is devoted to the effects of ion fluence on nanocrystal formation, as studied by TEM, selected area electron diffraction (SAD), and electronic transport measurements. The structure of the films before and after annealing is discussed, as well as the relationship between structure and electronic transport. Following implantation, an amorphous layer is formed. Following RTA at 600ºC, the low and medium fluence films have recrystallized into a single crystal GaAs layer while the high fluence film has recrystallized into a polycrystalline layer. Hall measurements indicate a reduction in free carrier concentration following implantation due to the formation of defects which trap electrons. This reduction in free carriers leads to an increase in both the Seebeck coefficient and resistivity. Through this work, we identified the ion fluence necessary to

maximize the retained In concentration following implantation. Utilizing these results, the second portion of this chapter focuses on the influence of annealing temperature on nanocrystal formation and their effects on the thermoelectric properties. RTA at 450ºC leads to the nucleation of metallic In nanocrystals within a polycrystalline GaAs layer. These In nanocrystals act as electron donors, increasing the free carrier concentration in comparison to those films annealed at higher temperatures. The increase in interfacial density serves to scatter more phonons, decreasing the thermal conductivity by ~50% in comparison to bulk GaAs.

Chapter 4 presents investigations into the formation of Bi nanocrystals within GaAs. We study the effect of ion fluence on the formation of Bi nanocrystals and thermoelectric properties of the GaAs films, and discuss the role of microstructure on the electrical and thermal conductivity of the GaAs:Bi films through a comparison with GaAs:In and GaAs:N films. Following Bi implantation, the microstructure consists of a-GaAs with or without crystalline remnants, voids, and/or ripples. Following rapid thermal annealing (RTA), all layers have transformed to single crystal GaAs with embedded Bi NCs. For all Bi^+ fluences, κ is reduced by ~30% in comparison to that of GaAs, presumably due to phonon scattering at Bi NC/GaAs matrix boundaries. We have demonstrated a general trend of n and σ reduction following ion-implantation, while RTA yields a partial recovery of n and σ, as well as a reduction in κ due to phonon scattering. Finally, in Chapter 5, we present a summary and an outline for future work.

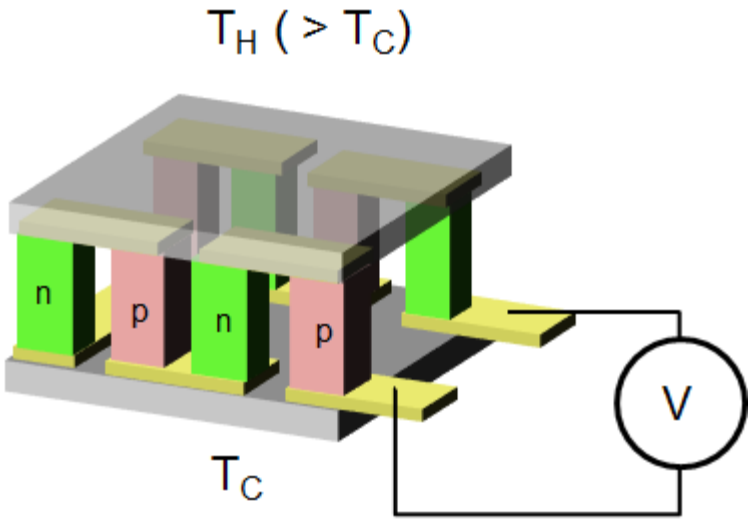

Fig. 1.1 Schematic representation of a thermoelectric device. The ceramic plates are marked in gray, while the metal contacts connecting adjacent semiconductor legs are marked in gold. The *n*- and *p*-type semiconductor legs are marked in green and pink, respectively.

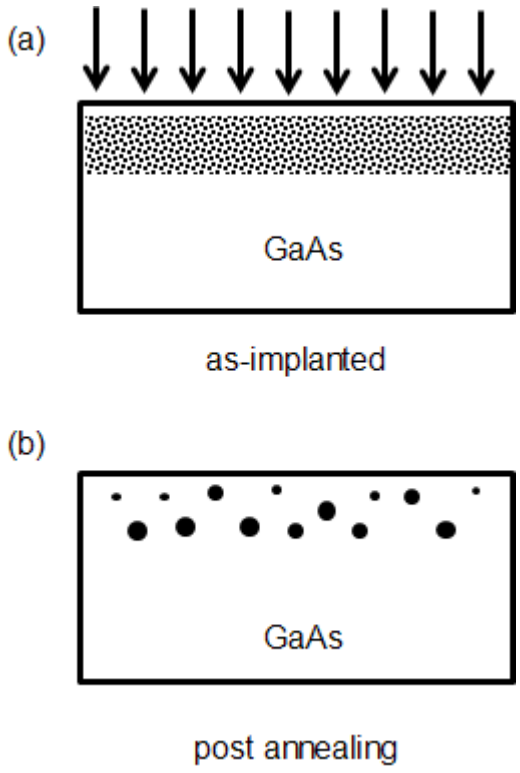

Fig. 1.2 Ion beam synthesis of nanostructures. In (a), a high ion fluence (~10^{16} cm^{-2} at 100 keV) is implanted into an epitaxial GaAs film to produce a supersaturated "amorphous" layer. In (b), after thermal annealing, nano-scale crystallites form within the disordered matrix.

1.7 Reference

[1] L.D. Hicks and M.S. Dresselhaus, Phys. Rev. B **47**, 12727 (1993).

[2] R. Venkatasubramanian, E. Siivola, T. Colpitts, and B. O'Quinn, Nature **413**, 597 (2001).

[3] M. Takashiri, K. Miyazaki, S. Tanaka, J. Kurosaki, D. Nagi, and H. Tsukamoto, J. Appl. Phys. **104**, 084302 (2008).

[4] M. Zebarjadi, G. Joshi, G. Zhu, B. Yu, A. Minnich, Y. Lan, X. Wang, M. Dresselhaus, Z. Ren, and G. Chen, Nano Lett. **11**, 2225 (2011).

[5] J.M. Zide, D.O. Klenov, S. Stemmer, A.C. Gossard, G. Zeng, J.E. Bowers, D. Vashaee, and A. Shakouri, Appl. Phys. Lett. **87**, 112102 (2005).

[6] J.P. Heremans, C.M. Thrush, and D.T. Morelli, J. Appl. Phys. **98**, 063703 (2005).

[7] D.M. Rowe, *CRC Handbook of Thermoelectrics*, CRC Press, 1995, pp. 1-5.

[8] H.J. Goldsmid and R.W. Douglas, Br. J. Appl. Phys. **5**, 386 (1954).

[9] T.M. Tritt and M.A. Subramanian, MRS Bull. **31**, 188 (2006).

[10] J. Yang and T. Caillat, MRS Bull. **31**, 224 (2006).

[11] G.S. Nolas and H.J. Goldsmid, *Thermal Conductivity: Theory, Properties, and Applications*, T.M. Tritt, Ed., Kluwer Academic/Plenum, New York, 2004, p. 106.

[12] G.D. Mahan and J.O. Sofo, *Proc. Natl. Acad. Sci. U.S.A.* **93**, 7436 (1996).

[13] M.S. Dresselhaus, G. Chen, M.Y. Tang, R. Yang, H.Lee, D. Wang, Z. Ren, J.P. Fleurial, and P. Gogna, *Adv. Materl.* **19** 1043 (2007).

[14] L. D. Hicks and M. S. Dresselhaus, *Phys. Rev. B* **47**, 16631 (1993).

[15] L.D. Hicks, T.C. Harman, X. Sun, and M.S. Dresselhaus, *Phys. Rev. B* **53**, R10493 (1996).

[16] S.V. Faleev and F. Léonard, *Phys. Rev. B* **77**, 214304 (2008).

[17] R. Koltun, J.L. Hall, T.E. Mates, J.E. Bowers, B.D. Schultz, and C.J. Palmstrøm, J. Vac. Sci. Technol. B **31**, (2013).

[18] A. Yadav, K. Pipe, W. Ye, and R. S. Goldman, *J. Appl. Phys.* **105**, 093711 (2009).

[19] V. M. Fomin, and P. Kratzer, *Phys. Rev. B* **82**, 045318 (2010).

[20] A. I. Boukai, Y. Bunimovich, J. Tahir-Kheli, J. K. Yu, W. A. Goddard III, and J. R. Heath, *Nature* **451**, 168 (2008).

[21] R. Srinivasan and K. Ramachandran, *Cryst. Res. Technol.* **43**, 953 (2008).

[22] M. Zebarjadi, K. Esfarjani, Z. Bian, A. Shakouri, *Nano Lett.* **11**, 225 (2011).

[23] X.W. Wang, H. Lee, Y.C. Lan, G.H. Zhu, G. Joshi, D.Z. Wang, J. Yang, A.J. Muto, M.Y. Tang, J. Klatsky, S. Song, M.S. Dresselhaus, G. Chen, and Z.F. Ren, Appl. Phys. Lett. **93** 193121 (2008).

[24] B. Poudel, Q. Hao, Y. Ma, Y. Lan, A. Minnich, B. Yu, X. Yan, D. Wang, A. Muto, D. Vashaee, X. Chen, J. Liu, M.S. Dresselhaus, G. Chen, and Z. Ren, Science **320**, 634 (2008).

[25] H. Beyer, J. Nurnus, H. Bottner, A. Lambrecht, E. Wagner, and G. Bauer, Phys. E Low-Dimens. Syst. Nanostructures **13**, 965 (2002).

[26] Y.K. Koh, C.J. Vineis, S.D. Calawa, M.P. Walsh, and D.G. Cahill, Appl. Phys. Lett. **94**, 153101 (2009).

[27] B. Daudin, F. Widmann, G. Feuillet, C. Adelmann, Y. Samson, M. Arlery, and J. L. Rouviere, *Mater. Sci. Eng. B,* **50**, 8 (1997).

[28] A. Meldrum, R. F. Haglund, Jr., L. A. Boatner, and C. W. White, *Adv. Mater*. **13**, 1431 (2001).

[29] E. Rimini, "Ion implantation: basics to device fabrication" (Kluwer Acad. Pub. Boston, MA, 1995).

[30] C. W. White, A. Meldrum, J. D. Budai, S. P. Withrow, E. Sonder, R. A. Zuhr, D. M. Hembree, M. Wu, D. O. Henderson, *Nucl. Instrum. Methods B* **148**, 991 (1999).

[31] K. H. Heinig, B. Schmidt, A. Markwitz, R. Grötzschel, M. Strobel, S. Oswald, *Nucl. Instrum. Methods B* **148**, 969 (1999).

[32] T. Shimizu-Iwayama, M. Oshima, T. Niimi, S. Nakao, K. Saitoh, T. Fujita, N. Itoh, *J. Phys.: Condens. Matter* **5**, 375 (1993).

[33] C.W. White, J.D. Budai, S.P. Withrow, J.G. Zhu, E. Sonder, R.A. Zuhr, A. Meldrum, D.M. Hembree, Jr, D.O. Henderson, and S. Prawer, Nucl. Instrum. Methods Phys. Res. Sect. B Beam Interact. Mater. At. **141**, 228 (1998).

[34] K. Radermacher, S. Mantl, C. Dieker, and H. Lüth, Appl. Phys. Lett. **59**, 2145 (1991).

[35] H.A. Atwater, K.V. Shcheglov, S.S. Wong, K.J. Vahala, R.C. Flagan, M.L. Brongersma, and A. Polman, MRS Proc. **316**, (1993).

[36] D. Matsuura, Y. Kanemitsu, T. Kushida, C.W. White, J.D. Budai, and A. Meldrum, Appl. Phys. Lett. **77**, 2289 (2000).

[37] X. Weng, W. Ye, S. J. Clarke, R. S. Goldman, V. Rotberg, A. Daniel, and R. Clarke, *J. Appl. Phys*. **97**, 064301 (2005).

[38] X. Weng, S. J. Clarke, W. Ye, S. Kumar, A. Daniel, R. Clake, J. Holt, J. Sipowska, A. Francis, V. Rotberg, and R. S. Goldman, *J. Appl. Phys*. **92**, 4012 (2002).

Chapter 2

Experimental Procedures

2.1 Overview

This chapter describes the experimental methods used to synthesize and characterize the nanostructures studied in this thesis. For these experiments, epitaxial GaAs films grown on semi-insulating (001) GaAs substrates were broad-area irradiated with either In^+ or Bi^+ ions. Following implantation, the films were subjected to rapid thermal annealing (RTA) for 30 s at a variety of temperatures. Transmission electron microscopy (TEM) imaging and electron diffraction were carried out in a JEOL 3011 operating at 300 kV. Energy Dispersive X-Ray Spectroscopy (EDX) mapping and high-angle annular dark field (HAADF) scanning transmission electron microscopy (STEM) were performed in a JEOL 2010 TEM operating at 200 kV.

The thermoelectric properties of these films were measured via a variety of transport measurements. Hall measurements in a van der Pauw geometry were utilized to assess the free carrier concentration at various stages of sample processing. The temperature dependence of the resistivity and Seebeck coefficient of the films was measured using a rectangular geometry. The thermal conductivity was measured using a pump-probe spectroscopy technique termed time-domain thermoreflectance (TDTR).

2.2 Molecular Beam Epitaxy (MBE)

The In and Bi nanostructures described in the thesis were synthesized within epitaxial GaAs layers, grown in a Modified Varian Gen II MBE system. Molecular beam epitaxy (MBE) is a vacuum deposition technique used to prepare high quality epitaxial films one atomic layer at a time.[1,2] In an ultra-high vacuum chamber, molecular beams are produced by sublimating or evaporating heated solids or liquids, which chemically react on a substrate surface, to form an epitaxial film.[3] Growth conditions far from equilibrium can be achieved because the incoming molecules are reactive,.

The Modified Varian Gen II chamber consists of separately pumped growth, buffer, and load-lock chambers connected by magnetic transfer rods and trolleys, as shown schematically in Fig. 2.1. The growth chamber source flange houses 7 solid sources (Ga, Al, In, Si, Be, Bi and an As cracker). These source materials are held within pyrolytic boron nitride (PBN) crucibles located in Knudsen effusion cells. The molecular beam flux is exponentially dependent on the source material temperature, which is controlled by heating filaments wrapped around the crucibles and monitored by a thermocouple in contact with the crucible. An ionization gauge sitting at the growth position measures the beam flux. Computer controlled pneumatic shutters are used to control the exposure of each molecular beam. The As flux is controlled with a needle valve in front of the As cell, which can be adjusted between 0 and 300 mil. Samples are held in the growth position by a manipulator referred to as the CAR (for Continuous

Azimuthal Rotation). The CAR is rotated during growth to improve the uniformity of the film grown. The growth chamber pressure is monitored via another ionization gauge on the side wall. During idling, the base pressure of the chamber is ~$2x10^{-9}$ Torr, which drops to <$3x10^{-10}$ Torr when liquid nitrogen (LN_2) is flowing through the cryoshrouds. During growth, the chamber pressure rises to ~ $1x10^{-8}$ Torr.

All films were grown on "epi-ready" GaAs substrates, which arrive in a dry N_2 sealed container, ready for immediate introduction into the load-lock. All substrates were indium-mounted on heated molybdenum blocks, prebaked at 150ºC for 8 hours in the load-lock, then outgassed for 30 min at 180ºC in the buffer chamber. In the growth chamber, the substrate temperature was raised to 300ºC, at which point, the As_2 shutter and needle valve were opened, providing an As_2 overpressure of ~$5x10^{-6}$ Torr. The substrate temperature was then continuously raised until a reflection high-energy electron diffraction pattern transitions from diffuse rings to a streaky pattern, indicative of a desorption of the surface oxide. Oxide desorption from GaAs has been reported to occur in the range of 580 to 610ºC.[4,5] The corresponding measured substrate temperature, measured via thermocouple, ranged from 750 to 830ºC. The oxide desorption temperature was used as an internal block calibration for each growth due to the substrate temperature thermocouple being in contact with the backside of each molybdenum block. Following oxide desorption, the block temperature was then increased an additional 30ºC and outgassed for 5 minutes to ensure that the surface oxide was completely desorbed.

2.3 Broad-Area Ion Implantation

The In and Bi nanostructures studied in this thesis were synthesized utilizing broad-area ion implantation of In^+ and Bi^+, respectively, followed by rapid thermal annealing (RTA). All implantations were performed at the Michigan Ion Beam Laboratory (MIBL), using an NEC 400kV Ion Implanter. A schematic of the broad-area ion implanted used in these studies in presented in Fig. 2.2. The major components are the ion source, a mass separation system, the accelerating column, and a scanning system.[6] The ion source contains the species to be implanted and an ionizing system to ionize the species. In the case of indium and bismuth, a plasma is created with argon gas which sputters atoms from indium-tin-oxide and bismuth-oxide sources, respectively. These atoms are then ionized and the ions are extracted from the source by a small accelerating voltage and then accelerated into the mass separation system. Here, the ions are subjected to a Lorentz force, resulting in a spatial separation of ions dependent on the differences in their masses and charges. By tuning the Lorentz force, the desired ion species are separated from all others, such as residual air, hydrocarbons from vacuum pumps, and other impurities. At the outlet of the mass separation system is the accelerating column which accelerates the ion beam by a static electric field. Since the ion beam size is often smaller than the target area to be implanted, the ion beam is rastered over the whole implantation area. This is realized by electrostatic fields between the X-Y deflector plates. At the target, the ion beam finally impinges on the wafer.

For all samples discussed in this thesis, implantation into 500 nm thick GaAs films (Si doped) grown by MBE as described above, was performed. The films were

implanted with 100 keV In^+ and Bi^+ at fluences of $3.8x10^{15}$ to $3.8x10^{17}$ cm^{-2} and $1.4x10^{16}$ to $5.6x10^{16}$ cm^{-2} with calculated projected ranges[7] of 35 and 27 nm, respectively. To minimize channeling, a ~7° ion beam angle of incidence with respect to the sample surface normal was utilized. During implantation, the substrate temperature was maintained at 77 K.

2.4 Rapid Thermal Annealing (RTA)

RTA experiments in this thesis were carried out using a JetFirst – 150 RTA system at the Solid-State Electronic Laboratory (SSEL) of Electrical Engineering and Computer Science Department in the University of Michigan. Presented in Fig. 2.3 is a diagram of the RTA system. During RTA, the sample is supported on a Si wafer and isolated from inside of the cell with quartz pins. The cell can be filled a controllable gas ambient. A tungsten-halogen lamp heats the sample through transparent windows coupled with highly reflective mirrors. The sample can be heated to ~1000°C for a time interval of 1 to 20 s. Samples in this thesis were annealed in flowing Ar gas at 450 to 600°C for 30 s.

2.5 Transmission Electron Microscopy Sample Preparation

Cross-sectional TEM (XTEM) was used to examine the microstructure of the GaAs:In and GaAs:Bi nanostructures. XTEM samples were prepared by mechanical

polishing followed by Ar ion milling at 77K, schematically shown in Fig. 2.4. For these samples, two pieces of ~1.5 x 3 mm were glued together epilayer side to epilayer side using Micro-Measurements M-Bond 610 epoxy. To prevent the epoxy from bonding the sample to the preparation surface, Teflon tape was used to wrap the sample preparation surface. The epoxied samples were cured for 2 hours at 100°C on a hot plate. This low curing temperature was chosen in order to avoid any unintentional sample annealing. After cooling in air, the samples were mechanically polished in cross-section using 600, 1000 and 1200 grit SiC papers in sequence. Following polishing of one side, the sample was mounted polish-side down on a 3 mm diameter slotted Mo grid (with a slot size of 1 x 2 mm) using the epoxy and curing process described above. The sample was then mechanically polished on the free side using the process described above, until a sample thickness of ~50 μm was reached, as determined with a Mitutoyo upright dial gauge. Finally, the samples were ion milled until a hole is formed using a Gatan ion miller. To minimize ion damage during milling, the samples were cooled to 77 K and low angles of incidence (3-6°) and low beam energies (3-5 kV) were used.

2.6 Transmission Electron Microscopy (TEM)

To study the evolution of the GaAs:In and GaAs:Bi microstructures, transmission electron microscopy (TEM) was utilized, both before and after annealing. We used diffraction contrast imaging and high-resolution TEM (HRTEM), which are described

below. All TEM experiments were conducted at the Michigan Electron Microbeam Analysis Laboratory (EMAL), using a JEOL 3011 microscope.

Conventional diffraction contrast TEM imaging was conducted using a JEOL 3011 transmission electron microscope operating at 300 keV. The microscope was frequently aligned in dark-field mode, such that only one set of diffracted beams is used for imaging. A schematic of the dark-field alignment is shown in Fig. 2.5. An objective aperture is used to select either the direct (000) or diffracted (hkl) beam to form a bright field (BF) images or dark field (DF) image, respectively. The contrast between the images is a result of the differences in intensities of electrons scattered into the diffracted beam from various parts of the sample and is consequently called "diffraction contrast".[8] Typically, diffraction planes used for imaging were the {220} reflections of GaAs but the {110} In reflection was also used. A detailed description of diffraction analysis techniques is presented in Appendix A.

To obtain HRTEM images, the sample was tilted such that the incident beam was aligned along the <110> zone axis. The objective aperture was inserted and positioned such that multiple beams were selected to form the HRTEM images. The contrast in the images is called "phase contrast," which arises due to the fact that the electrons exiting the bottom of the sample have small variations in phase arising from internal scattering inside the sample. The images were captured with Gatan Digital Micrograph through a CCD camera.

2.7 Energy Dispersive X-Ray Spectroscopy (EDX)

The chemical composition of implanted and annealed samples was examined qualitatively by Energy Dispersive X-Ray Spectroscopy (EDX), in a JEOL 2010 TEM operating at 200 keV. During electron beam irradiation, incident electrons will eject inner-shell electrons from their orbital. An outer-shell electron will then relax to a lower-energy state to occupy that vacant orbital, emitting an X-ray with energy equal to this difference in energy levels. This emitted X-ray is characteristic of the atomic structure of the excited atom, and the number of X-rays emitted in a given time correlate to the relative concentration of that element in the sample. In this case, a Si(Li) diode under reverse bias was used to detect the energies of emitted X-rays.

2.8 Hall and Resistivity Measurements

The electrical transport properties of the GaAs:In and GaAs:Bi films were determined by Hall and resistivity measurements in the van der Pauw geometry. A typical sample is shown in Fig. 2.6: a symmetric sample ~5 mm square with ~0.5 mm diameter contacts. In was deposited at the edges of the square sample, followed by annealing at 400ºC for 2 min in an N_2 atmosphere to fabricate the contacts. Gold wires 25 μm in diameter were soldered to the contacts using more In and connected to a component carrier. While straightforward to fabricate, van der Pauw geometry samples have two

intrinsic sources of error. First, due to the finite size of contacts, the error introduced in the resistance measurement is:

$$\frac{\Delta R_H}{R_H} = -\frac{8d}{\pi^2 D} \tag{2.1}$$

where R_H is the Hall coefficient, ΔR_H is the error in the Hall coefficient, d is the dimension of the contact, and D is the dimension of the sample.[9] The second source of error is due to the asymmetric shape of the sample. If the sample is not perfectly square, a correction factor needs to be considered as follows:

$$\rho_{real} = f \cdot \rho_{measured} \tag{2.1}$$

where $f \leq 1$ and depends on the degree of sample asymmetry.[9] For the samples presented in this work, the contact dimension was ~1 mm and the sample dimension was ~5 mm, with negligible asymmetry, resulting in a measurement error of ~ 16%. To determine the Ohmic nature of each contact, current-voltage measurements were performed with a Hewlett Packard 4156B semiconductor parameter analyzer. Typical contact resistances measured were on the order of 100 Ω, 1 kΩ, and 100 Ω for as-grown, ion-implanted, and implanted-plus-annealed samples, respectively. For Hall and resistivity measurements, a Keithley 224 current source was used to send a current ranging from 100 nA to 10 μA between two contacts. In the absence of an applied magnetic field, the voltage difference is measured parallel to the direction of current flow. Then, Hall measurements were performed by subjecting the sample to a ~0.124 Tesla magnetic field while passing an electrical current. Because the charge carriers are moving through a magnetic field, they are subjected to a Lorentz force and will drift in a direction perpendicular to both the current flow and magnetic field, resulting in a potential difference in this third direction,

termed the "Hall voltage." From these measurements, the resistivity and free carrier concentration were determined using the procedures in ASTM standard F76.[10]

2.9 Variable Temperature Seebeck and Resistivity Measurements

For variable temperature measurements of the Seebeck coefficient, $S = \Delta V/\Delta T$, samples were cleaved in 2 x 12 mm rectangles and In contacts were applied in the center of the sample separated by ~2.5 mm, and across the ends of the sample's major axis. These contacts were then annealed at 400ºC for 2 min in an N_2 atmosphere. A thermocouple and gold wire were attached to the two center contacts in order to measure the temperature and voltage difference between the contacts. Because a temperature gradient along the sample is necessary for Seebeck measurements, a 1 kΩ metal foil resistor acting as a current-driven heater was attached to one end of the sample. A copper block is clamped to the other end of the sample to act as a sample holder and heat sink. Gold wires are then attached to both the copper block and the In contact at the end of the sample, acting as a current source and drain for resistivity measurements. A schematic of the sample is shown in Fig. 2.7. A temperature gradient was induced within the sample by passing a current through the heater. The temperature and potential difference at the center contacts were then measured, from which the Seebeck coefficient was calculated. To measure the resistivity, a current was passed through the sample and the potential difference between the two center contacts was measured. This potential difference and the sample geometry can be related to the resistivity via the following formula,

$$\rho = \frac{VA}{Id} \tag{2.1}$$

where ρ is the resistivity, V is the potential difference between the contacts, A is the cross-sectional area of the current-carrying portion of the sample, I is the current, and d is the separation between the contacts.

The cryostat used in these Seebeck and resistivity measurements is composed of four concentric shells: the outer-most shell is filled with liquid nitrogen to act as a thermal barrier to the environment, the second shell is filled with liquid helium, the third shell is under vacuum to thermally insulate the second shell from the final shell, and the final shell houses the sample. A needle valve is used to connect the liquid helium shell with the vacuum shell and allow the transfer of helium into the vacuum shell, changing the temperature in the sample shell. A heater and temperature sensor on the sample holder is utilized to control the sample chamber temperature, allowing the cryostat to reach temperatures between 2 and 300 K.

2.10 Time-Domain Thermoreflectance (TDTR) Measurements

The thermal conductivity, κ, of the GaAs:In and GaAs:Bi films was measured using a spectroscopic technique termed time-domain thermoreflectance (TDTR).[11] For these measurements, ~2 x 3 mm samples were cleaved from the films. The GaAs:In (GaAs:Bi) films then had a 5 nm Ni (Ti) layer deposited on the surface, on which 85 nm of Al were deposited. This Al layer acts as a heat transducer, heating under laser-irradiation and then transferring that heat to the sample. In this experiment, a 1550 nm

pump pulse is used to heat a transducer layer on the sample surface and a 100 fs (780 nm) probe pulse is used to measure its reflectance, shown schematically in Fig. 2.8. For the analysis, we solved the time-dependent heat conduction equation,[12] assuming heat loss in the transducer and GaAs:In or GaAs:Bi layers, with $\kappa_{transducer} = \kappa_{Al} = 200$ W m^{-1} K^{-1}.[13] The calculated time-dependence of the reflectance is then fit with the experimental data using a least-squares minimization while varying the laser absorption depth, transducer-film boundary conductance, and κ_{film}.

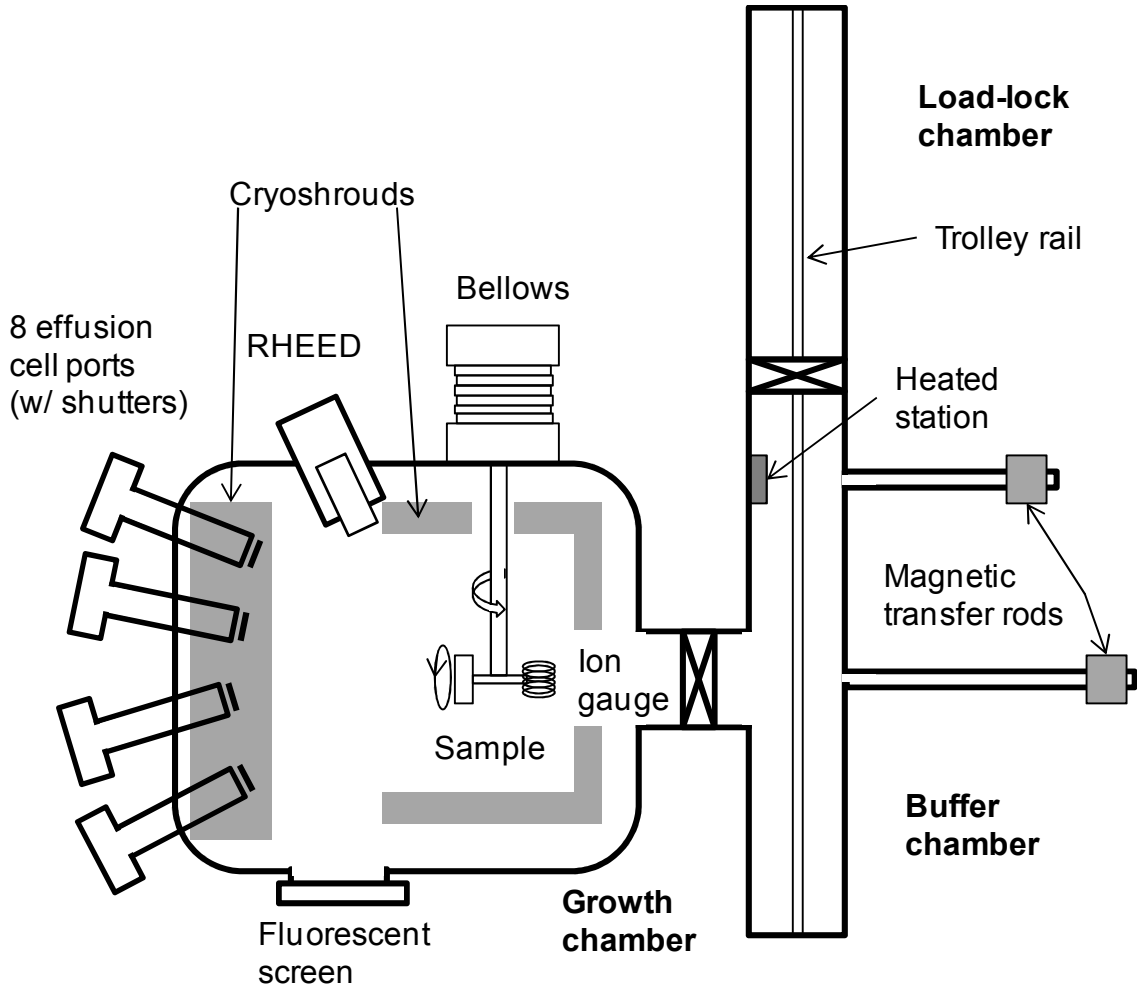

Fig. 2.1 Schematic of the Modified Varian Gen II molecular beam epitaxy system used in these studies. Seven solid sources are located in the effusion cell ports (Ga, Al, In, Si, Be, Bi and an As cracker).

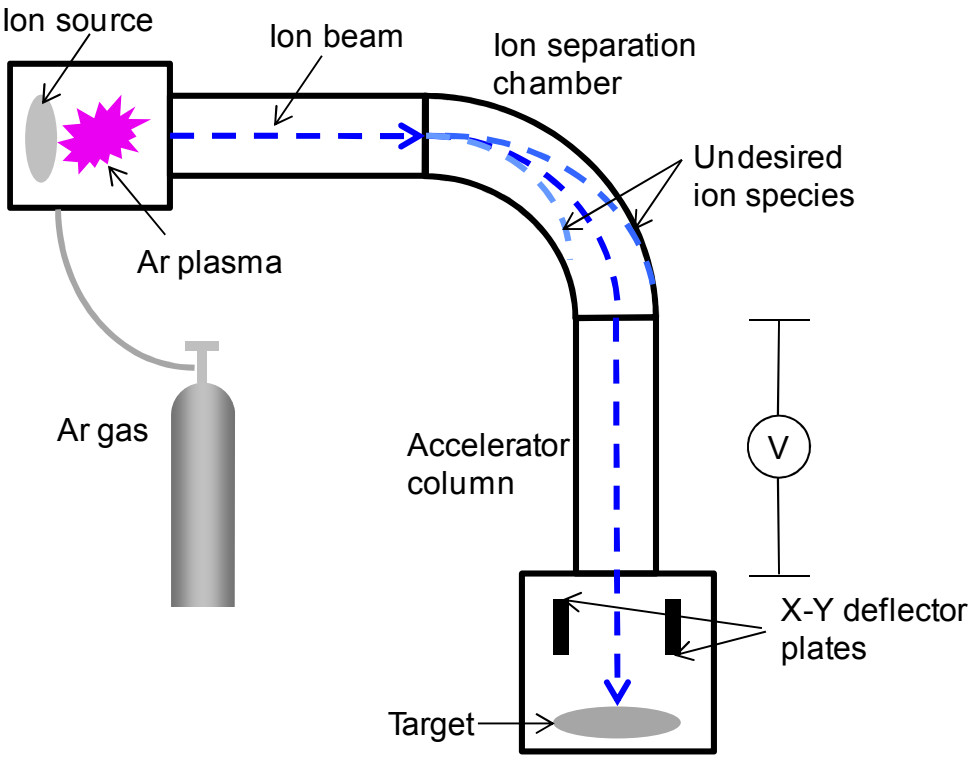

Fig. 2.2 Schematic of a typical ion implanter.

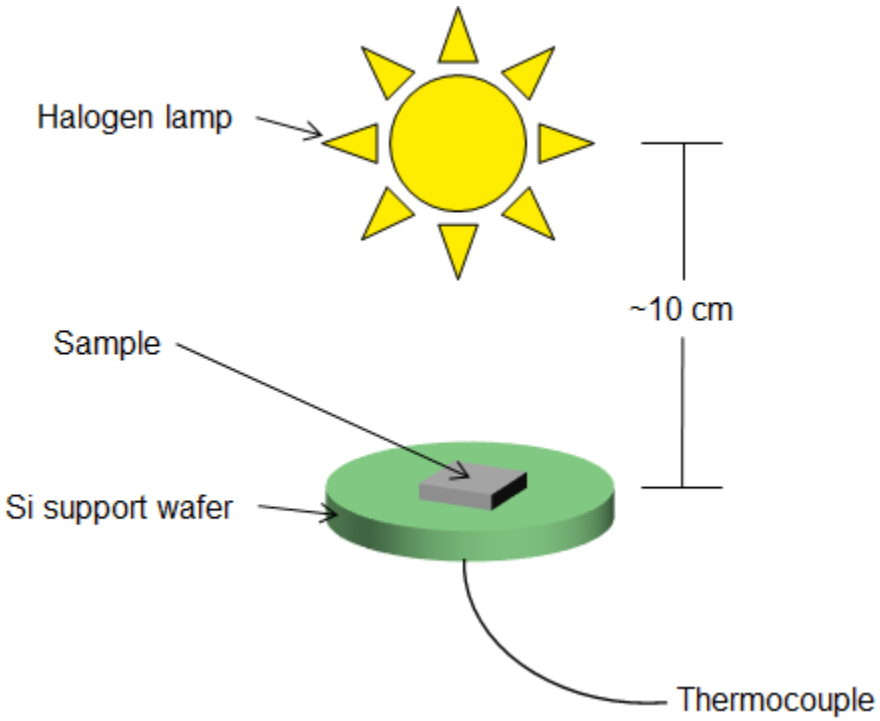

Fig. 2.3 Diagram of the rapid thermal annealing setup. The sample sits on a silicon wafer with a thermocouple contact on the underside. The chamber is purged with flowing nitrogen or argon gas and the sample is heated by a halogen lamp housed inside a quartz window.

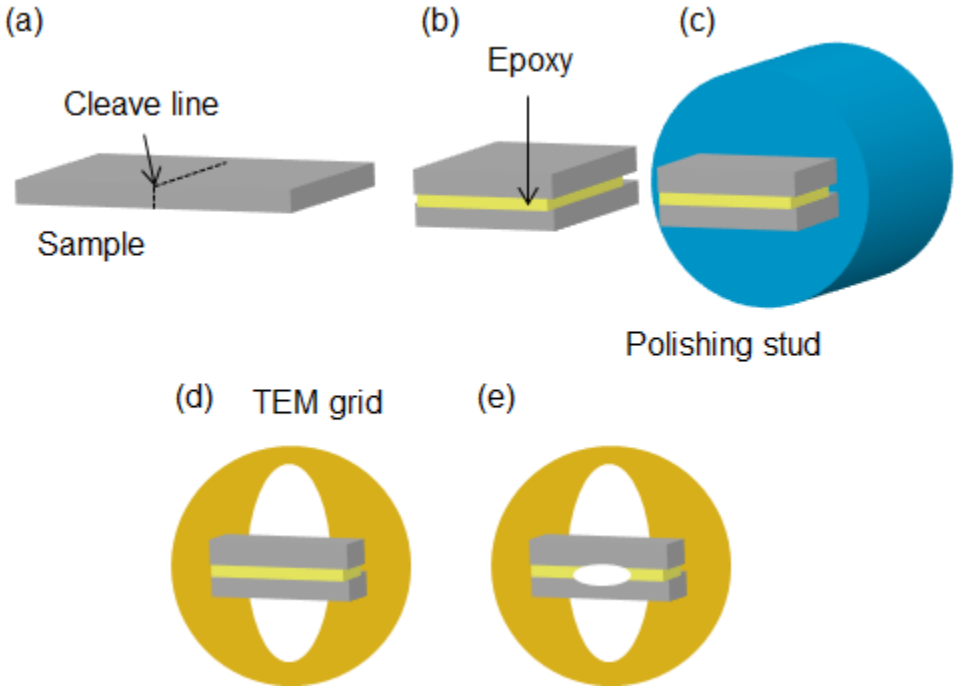

Fig. 2.4 Schematic of cross-sectional TEM sample preparation. The sample is (a) cleaved into two equal parts and (b) glued film side together using epoxy. The sample is then (c) mounted on a polishing stub and polished on one side before (d) mounting on a TEM grid with epoxy and polishing the opposite side to a final thickness of ~50 μm. The sample is then (e) placed in an Ar ion miller and milled until a perforation is formed in the center of the sample.

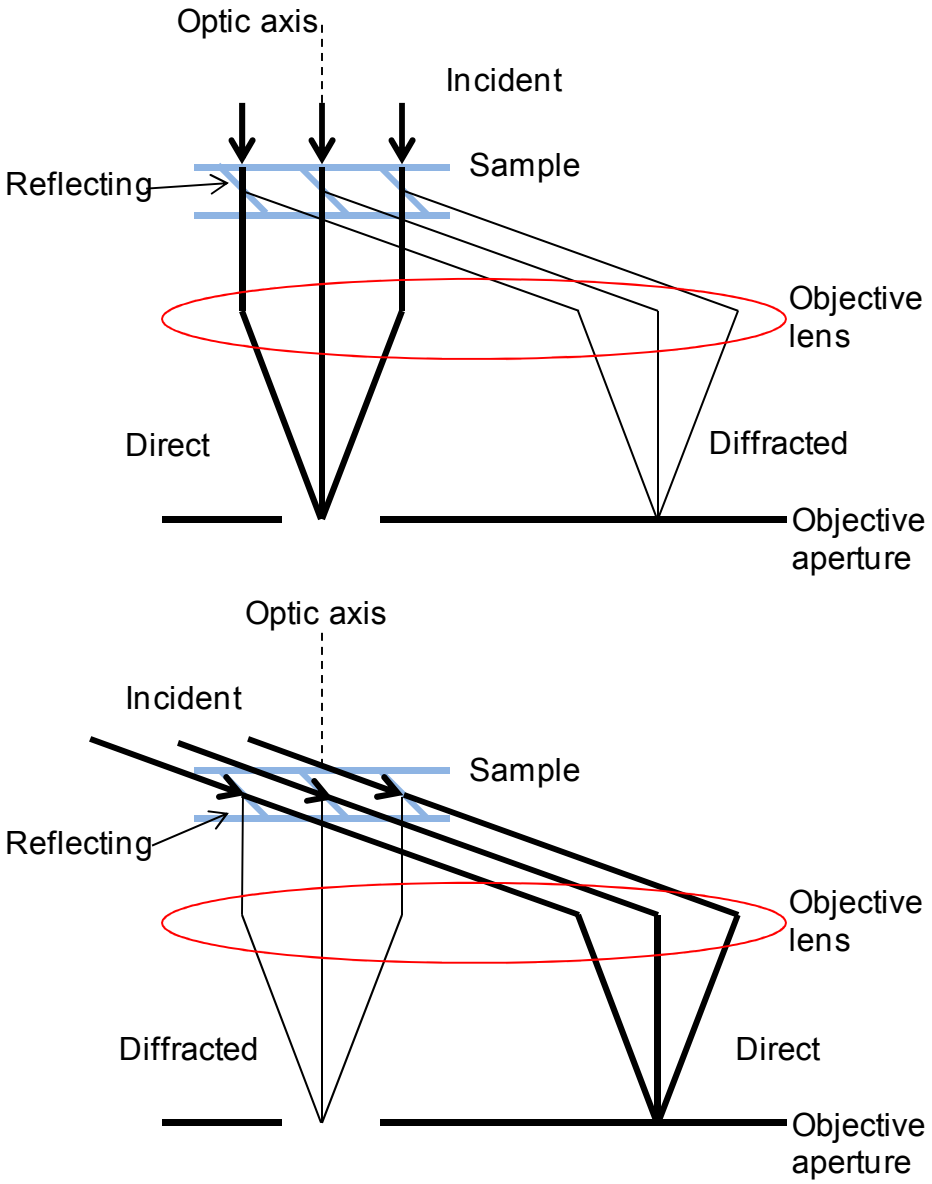

Fig. 2.5 Ray diagrams showing how the objective lens/aperture are used in combination to produce (a) a BF image from the direct beam and (b) a centered dark field image where the incident beam is tilted so that the scattered beam remains on axis. (Adapted from Ref. 8)

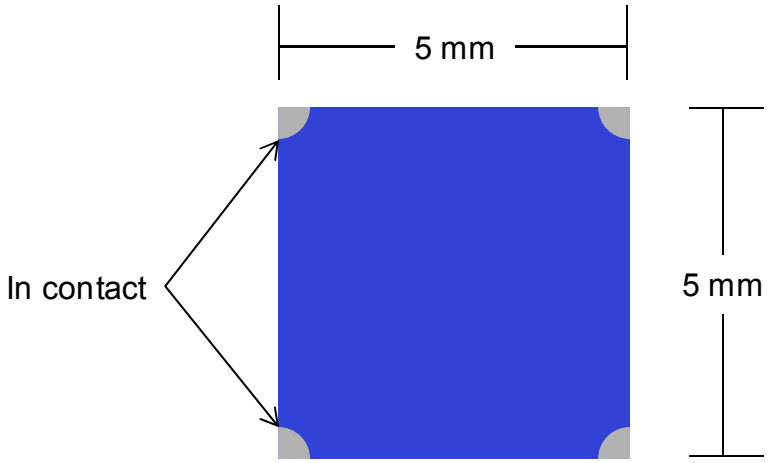

Fig. 2.6 The van der Pauw geometry used for resistivity and Hall measurements. In contacts are deposited at the corners of the sample.

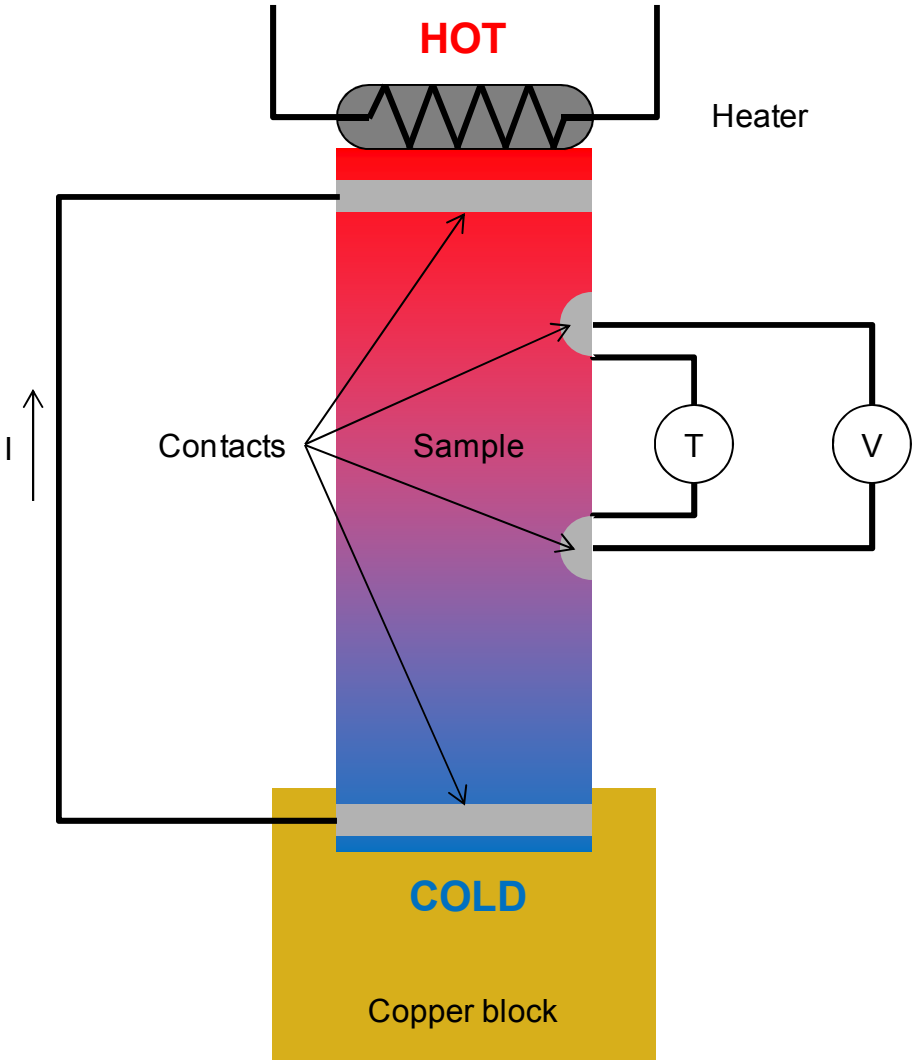

Fig. 2.7 Schematic sample setup for variable temperature Seebeck and resistivity measurements. For Seebeck measurements, a current is passed through the heater, while the copper block acts as a heat sink, inducing a temperature gradient. The temperature difference and Seebeck voltage are measured using the contacts on the side of the sample. For resistivity measurements, a current is passed from the top contact to the bottom, and the potential difference between the two side contacts is measured.

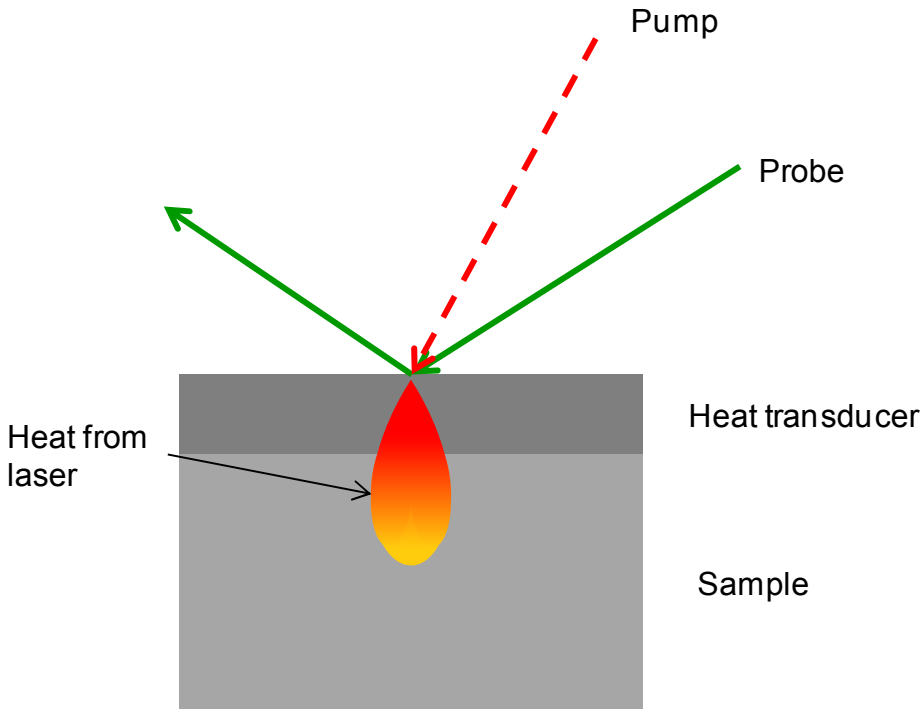

Fig. 2.8 Experimental setup for TDTR measurements. A 1550 nm pump pulse illuminates a metal heat transducer film on the surface of the sample. A 780 nm probe pulse is used to monitor the reflectance of the film as the heat equilibrates in the transducer and begins diffusing into the sample.

2.11 References

[1] A.Y. Cho and J.R. Arthur, Progr. Solid State Ch. **10**, 157 (1975).

[2] A.Y. Cho, J. Crys. Growth **202**, 1 (1999).

[3] C.T. Foxon and B.A. Joyce, *Growth and Characterisation of Semiconductors* (Adam Hilger, 1991) pp. 35.

[4] T. Vanbuuren, M.K. Weilmeier, I. Athwal, K.M. Colbow, J.A. Mackenzie, T. Tiedje, P.C. Wong and K.A.R. Mitchell, Appl. Phys. Lett. **59**, 464 (1991).

[5] A.J. Springthorpe, S.J. Ingrey, B. Emmerstorfer, P. Mandeville and W.T. Moore, Appl. Phys. Lett. **50**, 77 (1987).

[6] M. Nastasi, J. W. Mayer, and J. K. Hirvonen, eds. *Ion-solid Interactions: Fundamentals and Applications* (Cambridge University Press, Cambridge, UK, 1996), Chapter 2.

[7] J.F. Ziegler, J.P. Biersack, and U. Littmark, *The Stopping and Range of Ions in Matter* (Pergamon, New York, 1985).

[8] D. B. Williams and C. Barry Carter, eds. *Transmission Electron Microscopy* (Springer Science+Business Media, Inc. New York, 1996), Chapter 35.

[9] L. J. Van der Pauw, Philips Res. Repts. **26**, 220 (1958).

[10] ASTM Standard F76, "Standard Test Methods for Measuring Resistivity and Hall Coefficient and Determining Hall Mobility in Single-Crystal Semiconductors," ASTM International, West Conshohocken, PA, DOI: 10.1520/F0076-08.

[11] V.A. Stoica, Y.-M. Sheu, D.A. Reis, and R. Clarke, Opt. Express **16**, 2322 (2008).

[12] R.J. Stevens, A.N. Smith, and P.M. Norris, J. Heat Transfer **127**, 315 (2005).

[13] F. Cverna, *ASM Ready Reference: Thermal Properties of Metals* (ASM International, 2002), p. 341.

Chapter 3

Formation and Thermoelectric Properties of In Nanocrystals Embedded in GaAs

3.1 Overview

This chapter discusses our investigations into the formation of In nanocrystals (NCs) embedded in GaAs using ion beam synthesis similar to matrix-seeded growth.[1,2] This chapter opens with background information on studies of In^+ implantation into GaAs. This is followed by a section focused on our studies of the effect of In^+ fluence on NC formation. This section includes a description of the experiments used to characterize the films, followed by a discussion of the effects of implantation and annealing on the microstructure and thermoelectric properties. For the highest ion fluence, an enormous Seebeck coefficient of -12 mV/K is observed at 4 K.

The second section of this chapter is focused on the effect of annealing temperature on NC formation and the influence of these In NCs on the thermoelectric properties. This section also begins with a description of the experiments used in the characterization of the films, followed by a discussion of the formation of In NCs and their influence on the thermoelectric properties. The In nanocrystals enhance the free carrier concentration, while electron and phonon scattering at crystallite boundaries increases the resistivity and reduces the thermal conductivity. Furthermore, the room

temperature Seebeck coefficient exhibits a 25% increase due to carrier trapping. This chapter concludes with a summary.

3.2 Background

Nanocomposite materials have been identified as promising candidates for high figure-of-merit thermoelectric materials. Due to the increased control of the density of states and hence, the energies of charge carriers, nanocomposite materials are predicted to have a significantly higher thermoelectric figure-of-merit ($Z = S^2\sigma/\kappa$, where S is the Seebeck coefficient, σ is the electrical conductivity, and κ is the thermal conductivity) in comparison to their bulk counterparts.[3] For example, enhancements of Z due to low dimensionality have been reported for Bi_2Te_3/Sb_2Te_3 superlattices[4] and embedded Si nanocrystals in SiGe.[5] Additionally, it has been suggested that embedded metallic nanoparticles in a semiconducting matrix enhance its Seebeck coefficient via electron energy filtering.[6] Recently, a variety of embedded nanocrystals have been synthesized by matrix-seeded growth, which involves ion-beam-amorphization of a semiconductor film, followed by nanoscale recrystallization via rapid thermal annealing (RTA).[1,7] However, for the case of In^+ implantation, the relatively high sputter yield of GaAs leads to the replacement of a maximum of ~20% (Refs 8 and 9) of the original Ga atoms by In. Thus the predicted In-GaAs phase separation,[10] and subsequent formation of In NCs upon annealing, is unlikely. Therefore, to increase the retained In concentration, we have developed a "sputter-mask" method, based upon predictions from Profile Code

simulations (described in Appendix B), which involves implantation of various fluences of In^+ into GaAs layers covered with an *n*-type AlAs sputter-mask, followed by recrystallization initiated by rapid-thermal-annealing (RTA).

3.3 In Nanocrystal Formation and Properties: Effect of In^+ Fluence

3.3.1 Experiments

For these investigations, films were grown on semi-insulating (001) GaAs substrates using Ga, Al, As_2, and Si, as described elsewhere.[11] For both the reference and sputter-masked samples, a 500-nm-thick *n*-GaAs (Si doping, N ~ $5x10^{17}$ cm^{-3}) layer was grown at 580°C. For the sputter-mask samples, 50 nm of *n*-AlAs (Si doping, N ~ $5x10^{17}$ cm^{-3}) was then grown at 580°C. This free carrier concentration, *n*, is within 50% of the free carrier concentration predicted to maximize the GaAs power factor.[12] The sputter-mask samples were then implanted (as described in Chapter 2) with 100 keV In^+, at ion fluences of $3.8x10^{15}$, $3.8x10^{16}$, and $3.8x10^{17}$ cm^{-2}, which we will refer to as "low," "medium," and "high" fluence films, respectively. We note that the AlAs layers are expected to be partially (fully) sputtered away for the low and medium (high) fluence films. Following implantation, RTA was performed in Ar gas for 30 s at 600°C, using a GaAs proximity cap, intended to prevent As out-diffusion. Following growth and/or implantation and/or RTA, room temperature Hall effect measurements and the temperature-dependence of the resistivity, $\rho(T)$, and the Seebeck coefficient, $S(T)$, were

measured using the method described in Chapter 2. To examine the microstructure of the films, cross-sectional transmission electron microscopy (TEM) specimens were prepared using conventional mechanical polishing, followed by argon ion milling at 77 K. All selected area electron diffraction (SAD) patterns were calibrated to the GaAs substrate {110}.

3.3.2 Influence of Ion Fluence on Microstructure

Presented in Fig. 3.1 are typical bright-field TEM images of the as-implanted (a) low, (c) medium, and (e) high fluence films, with corresponding SAD patterns as insets. The low (medium) fluence films contain a 50 nm (6 nm) AlAs surface layer, with a 68 nm (143 nm) a-GaAs layer. The AlAs layer acts as a sputter-mask, preventing the sputtering of Ga and As atoms from GaAs during implantation. However, the high fluence film contains a ~100 nm a-GaAs surface layer with crystalline remnants. Due to the medium fluence film having the thinnest remaining sputter-mask, this fluence has been identified as the optimal fluence for maximizing the retained In concentration, as explained in Appendix B. Presented in Fig. 3.1(b), Fig. 3.1(d), and Fig. 3.1(f) are typical bright field TEM images, with corresponding SAD patterns as insets, of the annealed low, medium, and high fluence films, respectively. For the low (medium) fluence films, a 19 nm (10 nm) AlAs layer is present. Beneath this AlAs layer, a 100 nm (126 nm) recrystallized GaAs layer (labeled “R”) containing stacking faults (denoted with arrows) is observed. The stacking fault formation is likely due to simultaneous recrystallization of

the a-GaAs layer from the AlAs and crystalline GaAs interfaces. For the high fluence film, a polycrystalline GaAs layer without stacking faults is observed.

3.3.3 Influence of Ion Fluence on Resistivity and *n*

In Fig. 3.2, we consider $\rho(T)$ for the low, medium, and high ion fluence films, in comparison with that of the GaAs reference. We note that for all ion fluences, the T-dependence of ρ is similar for both as-implanted and post-RTA films. For the GaAs reference, ρ is independent of T, indicating electron scattering via a combination of ionized impurities and lattice defects.[13] For all low and medium ion fluence films, ρ is similarly independent of T, indicating similar scattering mechanisms. However, the low and medium fluence films exhibit ρ values one to two orders of magnitude larger than those of the reference film. For the high fluence film, the T-dependence of ρ differs from that of the GaAs reference. Shown in the inset of Fig. 3.2 is a plot of $\ln(\rho)$ vs $T^{-1/4}$ for the high dose films, in comparison with the medium dose film before RTA. The medium fluence film shows that $\ln(\rho)$ is independent of $T^{-1/4}$, while for $T > 40$ K, the high fluence films exhibit a linear dependence of $\ln(\rho)$ on $T^{-1/4}$, suggesting variable-range-hopping conduction.[14] Thus, for the high fluence films, it is likely that carriers hop between the crystallites shown in Fig. 3.1(e) and Fig. 3.1(f).

We now consider the effects of ion fluence and RTA on $\rho(T)$ and n. The GaAs reference shows the lowest ρ across all measurement temperatures (2 – 300 K), with a room temperature ρ (4.2×10^{-3} Ω cm) within 20% of literature values for similarly-doped

single crystal GaAs films.[15] For the GaAs:In films, ρ increases with increasing ion fluence, reaching an ultra-high ρ for the high fluence film. For the low (medium) fluence film, the room temperature carrier concentration is $1x10^{17}$ cm^{-3} ($4x10^{16}$ cm^{-3}), corresponding to a 80% (92%) decrease compared to the reference film, consistent with a mechanism in which implantation produces defects, which trap carriers and reduce n.[16] For the low and medium fluence films, following RTA, ρ is decreased in comparison to that of the as-implanted samples, remaining higher than that of the GaAs reference. The corresponding n has nearly doubled to $2x10^{17}$ and $1x10^{17}$ cm^{-3}, presumably due to the annealing out of carrier trapping defects. For the high fluence film following RTA, for T < 100 K (> 100 K), ρ is increased (unchanged).

3.3.4 Influence of Ion Fluence on Thermoelectric Properties

We have also examined the influence of implantation and RTA on the T-dependence of the Seebeck coefficient, $S(T)$, as shown in Fig. 3.3. $S(T)$ for the GaAs:In films with low and medium ion fluences, in comparison with that of the GaAs reference are shown in Fig. 3.3(a). For all films, S is negative, implying n-type conduction. Since $|S|$ typically increases with decreasing carrier concentration,[17] the increase in $|S|$ is attributed to the carrier trapping process described above. At the lowest temperatures (T < 10 K), all films exhibit a rapid increase of $|S|$ that peaks at ~10 K. For T > 10 K, $|S|$ rapidly decreases until a temperature of ~100 K. This T-dependence of S is a manifestation of a strong electron-phonon interaction, often referred to as the phonon-

drag effect. The position of the phonon-drag peak near 10 K is similar for both the low and medium fluence films. For T > 100 K, $|S|$ increases monotonically with T, due to electron diffusion driven by the temperature gradient. In this electron diffusion regime, $|S|$ is higher than that of GaAs for both the low and medium fluences, with RTA leading to a decrease in $|S|$, due to the increase in free carrier concentration mentioned above.

We now consider $S(T)$ of the as-implanted high fluence film in comparison with that of the as-implanted medium fluence film, both shown in Fig. 3.3(b).[18] We note that the scale of Fig. 3.3(b) is in mV/K as opposed to the μV/K scale used in Fig. 3.3(a). For the high fluence film, at the lowest temperatures (T < 10 K), S is negative with $|S|$ increasing rapidly with decreasing T until it reaches an enormous value of -12 mV/K at 4 K. We consider this low T behavior of S to be a manifestation of phonon-drag of electrons. According to Herring,[19] as the free carrier concentration decreases, the increase in $|S|$ due to the phonon-drag effect increases. Thus, our enormous phonon-drag peak is attributed to a decrease in the free carrier concentration, due to both the trapping of carriers by defects and the conversion of Si atoms from *n*- to *p*-type dopants, as will be discussed below. For T > 10 K, S becomes increasingly more positive, peaks near 15 K, and then monotonically decreases (while remaining positive) up to 300 K. The peak near 15 K is interpreted as a manifestation of the phonon-drag of holes. In the high fluence film, the sign conversion of S indicates the presence of both electron and hole charge carriers, with a transition from electrons as the majority charge carrier (S < 0, T < 10 K) to holes as the majority charge carrier (S > 0, T > 10 K). In this case, the AlAs (GaAs) layers are fully (partially) sputtered away. Due to the higher sputter yield of As, the GaAs surface becomes As-deficient, i.e. As vacancies (V_{As}) are formed.[20] We propose a

mechanism in which ion implantation causes Si atoms to be displaced from Ga sites to the implantation-induced V_{As}, leading to an *n*-type (Si_{Ga}) to *p*-type (Si_{As}) conversion. A similar mechanism for *n*-to-*p*-type conversion was reported for MeV ion implantation of various ions (H^+, Er^+, and Si^+) into GaAs.[2124]

In Fig. 3.4, we consider the *T*-dependence of the power factor of the low, medium, and high ion fluence films in comparison with that of the GaAs reference. The GaAs reference shows the highest power factor across all measurement temperatures (2 – 300 K), with a room temperature power factor comparable to literature values for similarly-doped single crystal GaAs films.[12] For the GaAs:In films, the power factor decreases with increasing ion fluence, with a significant reduction in power factor for the high fluence film. This decrease in power factor is attributed to the increase in resistivity shown in Fig. 3.2. The minimum in power factor for the high fluence film is attributed to the *n*-to-*p*-type conversion, which causes $S = 0$ V/K at 10 K. For the low and medium fluence films, following RTA, the power factor increases, remaining less than that of the GaAs reference.

3.4 In Nanocrystal Formation and Properties: Effect of Annealing Temperature

3.4.1 Experiments

For these investigations, films were grown on semi-insulating (001) GaAs substrates using Ga, Al, As_2, and Si, as described elsewhere.[11] All samples consisted of

an undoped GaAs buffer (500 nm thick), followed by Si-doped layers of GaAs (500 nm thick) and an AlAs sputter-mask (50 nm thick), all grown at 580°C. The target doping concentration was $1x10^{18}$ cm^{-3}, within 50% of the *n* predicted to maximize the GaAs power factor.[12] Following growth, a portion of the film was reserved as a reference sample, while the remainder was implanted with 100 keV In^{+}, at an ion fluence of $3.8x10^{16}$ cm^{-2}, as described in Chapter 2. At this fluence, the AlAs layer is expected to be partially sputtered away while maximizing the retained In concentration.[25] Following implantation, RTA was performed in Ar gas for 30 s at 450, 500, and 550°C, which we will refer to as "low," "medium," and "high" *T* annealed films, respectively. During RTA, a GaAs proximity cap was used to minimize As out-diffusion.

Following growth and/or implantation and/or RTA, the temperature-dependence of the resistivity, $\rho(T)$, and the Seebeck coefficient, $S(T)$, as well as the room temperature free carrier concentration of the films were measured utilizing the methods detailed in Chapter 2. The thermal conductivity of the films was measured using the time-domain thermoreflectance (TDTR) method described in Chapter 2. TDTR measurements were enabled by the deposition of a surface thermal transducer consisting of a 5 nm/ 85 nm Ni/Al layer.

To examine the microstructure of the films, cross-sectional TEM specimens were prepared using conventional mechanical polishing, followed by argon ion milling at 77 K. TEM imaging and SAD were carried out in a JEOL 3011 operating at 300 kV. Energy Dispersive X-Ray Spectroscopy (EDX) and high-angle annular dark field (HAADF) scanning transmission electron microscopy (STEM) were performed in a JEOL 2010 TEM operating at 200 kV.

3.4.2 Influence of Annealing Temperature on Microstructure

Presented in Fig. 3.5 are typical bright-field TEM images of GaAs:In (a) as-implanted and following RTA at (c) low, (e) medium, and (g) high temperatures. The corresponding SAD patterns are shown in Fig. 3.5(b), Fig. 3.5(d), Fig. 3.5(f), and Fig. 3.5(h). The as-implanted film consists of a 100 nm thick a-GaAs surface film, below which is crystalline GaAs. The medium (high) *T* annealed film consist of a 96 nm (89 nm) recrystallized GaAs layer containing stacking faults. For the low *T* annealed film, a 63 nm polycrystalline GaAs layer is present. SAD indicates diffracted spots with d-spacings of 2.46 Å, within 1% of the {002} interplanar spacing of In. We note that this polycrystalline structure is presumably due to the low annealing temperature, which prevents full crystallization of the amorphized layer.

Fig. 3.6 presents typical HAADF images of GaAs:In (a) as-implanted and following RTA at (c) low, (e) medium, and (g) high temperatures. The corresponding EDX elemental maps are shown in Fig. 3.6(b), Fig. 3.6(d), Fig. 3.6(f), and Fig. 3.6(h), with In, Ga, and Al atoms labeled in green, blue, and red, respectively. EDX reveals the formation of an 85 nm thick In-rich layer following implantation. The high *T* annealed film shows In diffusion towards the substrate, while the medium *T* annealed film shows In segregating towards the surface, forming a 100 nm thick layer. For the low *T* annealed film, however, In-rich clusters ~85 nm in diameter are observed, consistent with the In diffraction spots in Fig. 3.5(d).

For the low *T* annealed film, we further examined the microstructure using bright-/dark-field and high-resolution TEM. In Fig. 3.7, close-up views of the polycrystalline GaAs layers containing In-rich clusters are shown in the (a) bright-field, (b) dark-field, and (c) high-resolution images. The dark-field image in Fig. 3.7(b) was obtained using the In {110} diffraction spot. A ~13 nm diameter feature is circled in Fig. 3.7(a) – (c). Since the feature appears bright in Fig. 3.7(b), it is attributed to an In NC. We note that additional bright-field images spanning > 0.2 μm^2 reveal In NCs with sizes ranging from 10 to 20 nm. The high-resolution image in Fig. 3.7(c) reveals an In NC located at the boundary of multiple GaAs crystallites, each labeled "A," which presumably serves as a NC nucleation site.

3.4.3 Influence of Implantation and Annealing on Carrier Concentration

We now consider the effects of RTA on the room temperature (RT) free carrier concentration, *n*. For the reference film, $n = 7.0 \pm 1.1 \times 10^{17}$ cm^{-3}; following implantation, *n* decreases by ~70% to $2.0 \pm 0.3 \times 10^{17}$ cm^{-3}, consistent with a mechanism in which point defects arising from the implantation process trap carriers and reduce *n*.[16] For the low *T* annealed film, *n* rises to $4.0 \pm 0.6 \times 10^{17}$ cm^{-3}. However, the medium and high *T* annealed films show an increase of *n* to $2.4 \pm 0.4 \times 10^{17}$ and $2.1 \pm 0.3 \times 10^{17}$ cm^{-3}, respectively. It is interesting to note that the most significant increase in *n* occurs for the In NC-containing film, presumably due to the In NCs acting as electron donors, similar to the doping effect reported for ErAs particles in GaAs.[26]

3.4.4 Influence of In Nanocrystals on Thermoelectric Properties

Having established the formation of In NCs and their effect on n, we now investigate the effect of these NCs on the thermoelectric properties. In Fig. 3.8(a), we consider $\rho(T)$ for the low T annealed film, in comparison with that of the reference film. We note that the T-dependence of ρ is similar for both the low T annealed film and the GaAs reference. For both the GaAs reference and the low T annealed film, ρ is weakly dependent on T, indicating extended-band conduction.[13] However, the low T annealed film exhibits a ρ ~4.6 times higher than the GaAs reference, due to the changes in structure and n, described above.

We have also examined the influence of the In NCs on the T-dependence of the Seebeck coefficient, $S(T)$, as shown in Fig. 3.8(b), in comparison with that of the reference film. At the lowest temperatures ($T < 10$ K), both films exhibit a rapid increase of $|S|$ that peaks at ~10 K. For $T > 10$ K, $|S|$ rapidly decreases until a temperature of ~100 K. This T-dependence of S is a manifestation of a strong electron-phonon interaction, often referred to as the phonon-drag effect. The T-dependence of these films is similar to that of the films reported previously.[25] The position of the phonon-drag peak near 10 K is similar for both the low T annealed film and the GaAs reference. In this phonon-drag regime, $|S|$ of the low T annealed film is ~190 μV/K less than that of the GaAs reference. Presumably, the polycrystalline structure of the low T annealed film enhances phonon scattering, decreasing the likelihood of electron-phonon coupling, and therefore reducing

the magnitude of the phonon-drag peak. For $T > 100$ K, $|S|$ increases monotonically with T, due to electron diffusion driven by the temperature gradient. In this diffusion regime, the In NC-containing film exhibits higher values of $|S|$ than those of the reference, with ~50 μV/K difference at RT. This increase in $|S|$ is presumably due to free carrier trapping at implantation-induced defects, as described above, reduces n, thereby increasing $|S|$.

We have also examined the influence of the In NCs on the thermal conductivity, κ, of the films, using an analysis of TDTR measurements. Fig. 3.9 shows the time-dependence of the normalized reflectance for both the In NC-containing and reference GaAs films. During the first 100 ps, the metallic transducer is heated, leading to a rise in reflectance. From 200 to 4700 ps following the pump pulse, heat is dissipated through the In NC-containing (GaAs) layer in the nanocomposite (reference) film, leading to a gradual decrease in reflectance. For the analysis, we solve the time-dependent heat conduction equation,[27] assuming heat loss in the transducer and GaAs:In layers, with $\kappa_{transducer} = \kappa_{Al} = 200$ W m^{-1} K^{-1}.[28] The calculated time-dependence of the reflectance is then fit with the experimental data using a least-squares minimization while varying the laser absorption depth, transducer-film boundary conductance, and κ_{film}. In all cases, the laser absorption depth lies within the thickness of the transducer layer and the thermal boundary conductance is ~10^{17} W m^{-2} K^{-1}, similar to that reported for Al/GaSb.[29] For the reference film, $\kappa_{film} = 50$ W m^{-1} K^{-1}, similar to the reported value of $\kappa_{GaAs} = 55$ W m^{-1} K^{-1}.[30] For the In NC-containing film, $\kappa_{film} = 26$ W m^{-1} K^{-1}, ~50% of κ_{GaAs}. Thus, phonon scattering is increased in the In NC-containing film. As discussed above, In NCs are often located at the boundaries of multiple GaAs crystallites. Since the density of GaAs

crystallite-GaAs crystallite boundaries is higher than that of GaAs crystallite-In NC boundaries, phonons are likely primarily scattered at GaAs crystallite boundaries.

3.5 Conclusions

In summary, we have examined the microstructure and T-dependence of ρ, S, and the power factor of GaAs:In prepared by ion implantation followed by RTA. The low and medium fluence films consist of a residual AlAs layer on a-GaAs, whereas the high fluence film consists of an a-GaAs layer with crystalline remnants. Following RTA, the low and medium fluence films consist of a recrystallized GaAs layer with stacking faults likely due to simultaneous recrystallization from the AlAs and crystalline GaAs interfaces, while the high fluence film is polycrystalline. Both S and ρ increase with ion fluence, with the high fluence film showing both electrons (T < 10 K) and holes (T > 10 K) as charge carriers with corresponding phonon drag peaks of -12 mV/K at 4 K and +2 mV/K at 15 K. This sign conversion of S indicates an n-to-p-type conversion, presumably due to the migration of Si dopant atoms from Ga to As sites. For the low and medium (high) fluence films before and after RTA, ln(ρ) is independent (dependent) on $T^{-1/4}$, indicative of extended-band (variable-range-hopping) conduction. For the high fluence film, it is likely that charge carriers hop between crystallites. These results suggest a new path for the formation of embedded semiconductor nanocomposites for thermoelectrics.

This work then formed the basis of a study devoted to determining the annealing conditions necessary to nucleate In NCs within a GaAs matrix and examining the

influence of embedded In NCs on n, ρ, S, and κ of GaAs. Implantation amorphizes the surface of the GaAs film, inducing defects which trap carriers and reduce n. RTA at high and medium T results in a recrystallized GaAs film, while RTA at low T leads to a polycrystalline GaAs containing 10-20 nm diameter In NCs which act as electron donors. The GaAs crystallite boundaries serve to scatter electrons and phonons, increasing ρ and reducing κ. Furthermore, the room temperature Seebeck coefficient exhibits a 25% increase, presumably due to carrier trapping. Together, these data reveal that In NCs enhance n and S while decreasing σ. It is anticipated that application of this approach to more heavily doped GaAs layers will lead to NC-containing films with n similar to the optimum carrier concentration of GaAs, maximizing the thermoelectric power factor, $S^2\sigma$.

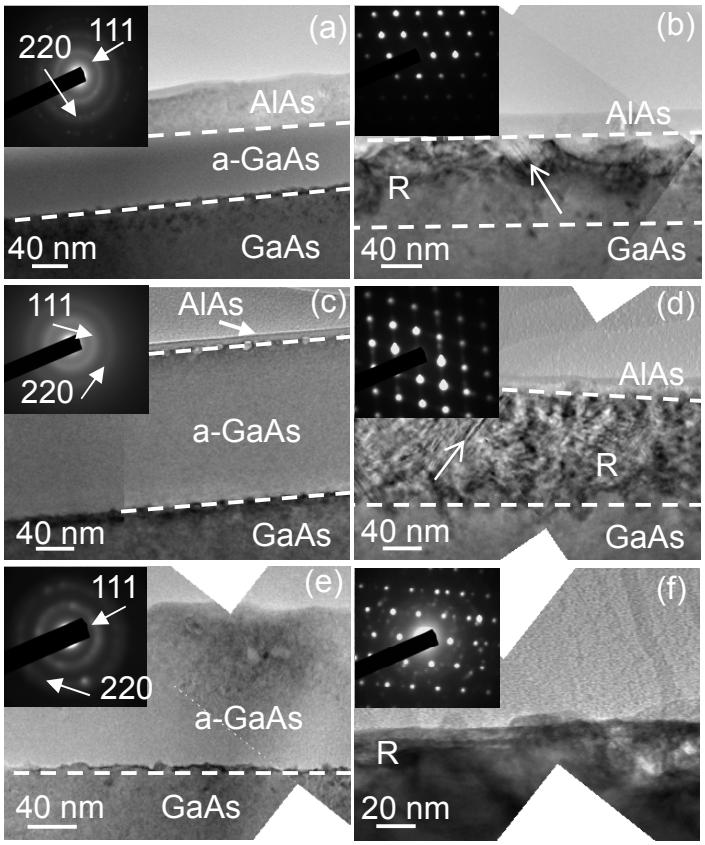

Fig. 3.1 Bright-field TEM images of low (a and b), medium (c and d), and high (e and f) ion fluence films both as-implanted and following RTA, respectively. The inset in (a)-(f) are the corresponding SAD patterns. Before RTA, the (a) low and (c) medium fluence films consist of an AlAs layer on top of a-GaAs, whereas, the (e) high fluence film consists of an a-GaAs layer containing crystalline remnants. Following RTA, the (b) low and (d) medium fluence films show recrystallization of the a-GaAs (region labeled "R") with stacking faults present (denoted by arrows), while the (f) high fluence film has recrystallized into a polycrystalline layer.

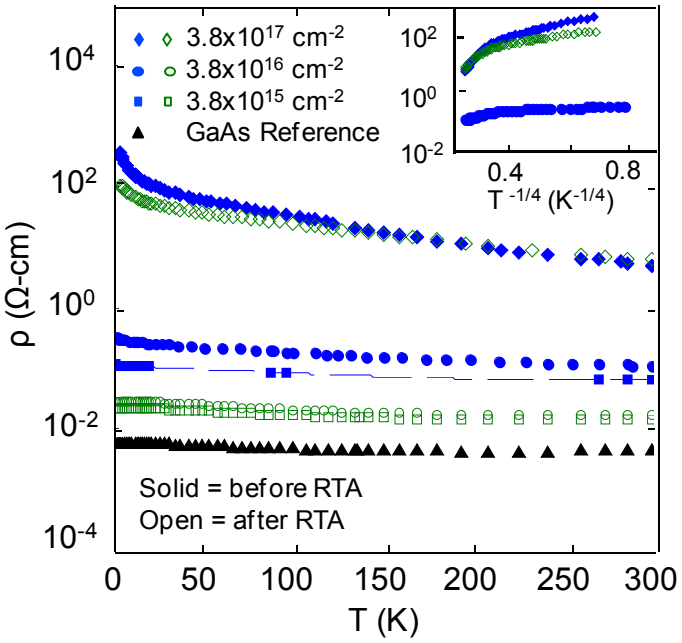

Fig. 3.2 Resistivity, ρ, as a function of temperature for GaAs:In films with low, medium, and high ion fluences (as-implanted and after RTA) in comparison to that of a GaAs reference. For most samples, ρ is T-independent, suggesting electron scattering via a combination of ionized impurities and lattice defects. However, the high fluence films show a deviation from this T-independence. The inset contains a plot of $\ln(\rho)$ as a function of $T^{-1/4}$ for both the high fluence films and the medium fluence film before RTA. For the medium fluence film, $\ln(\rho)$ is independent of $T^{-1/4}$, while the high fluence films exhibit a linear dependence of $\ln(\rho)$ on $T^{-1/4}$ for $T > 40$ K, suggesting variable-range-hopping conduction.

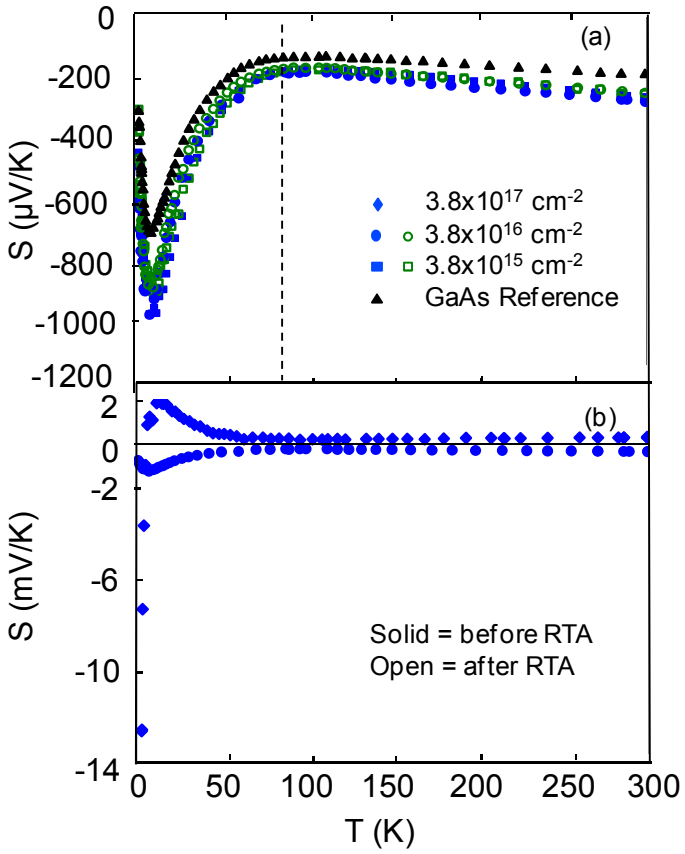

Fig. 3.3 (a) Seebeck coefficient, S, as a function of temperature for GaAs:In films with low and medium ion fluences (both as-implanted and following RTA), in comparison to that of the GaAs reference. The enhancement in $|S|$ for $T < 100$ K is attributed to phonon drag. The monotonic increase in $|S|$ from 100 K to 300 K is due to electron diffusion driven by the T gradient. (b) $S(T)$ for as-implanted GaAs:In films with medium and high ion fluences. For $T < 10$ K (> 10 K), S is negative (positive), implying a n-to-p-type carrier conversion.

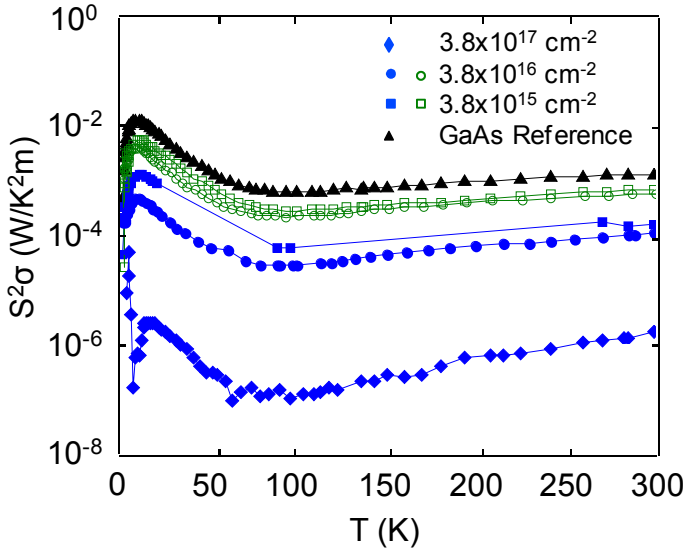

Fig. 3.4 Power factor ($S^2\sigma$) as a function of temperature for GaAs:In films with low, medium, and high ion fluences (as-implanted and after RTA) in comparison to that of a GaAs reference. In comparison to the reference film, the power factor of the implanted films decreases with increasing implantation fluence. Following RTA, the power factor of the low and medium fluence films increases, remaining less than that of the reference film.

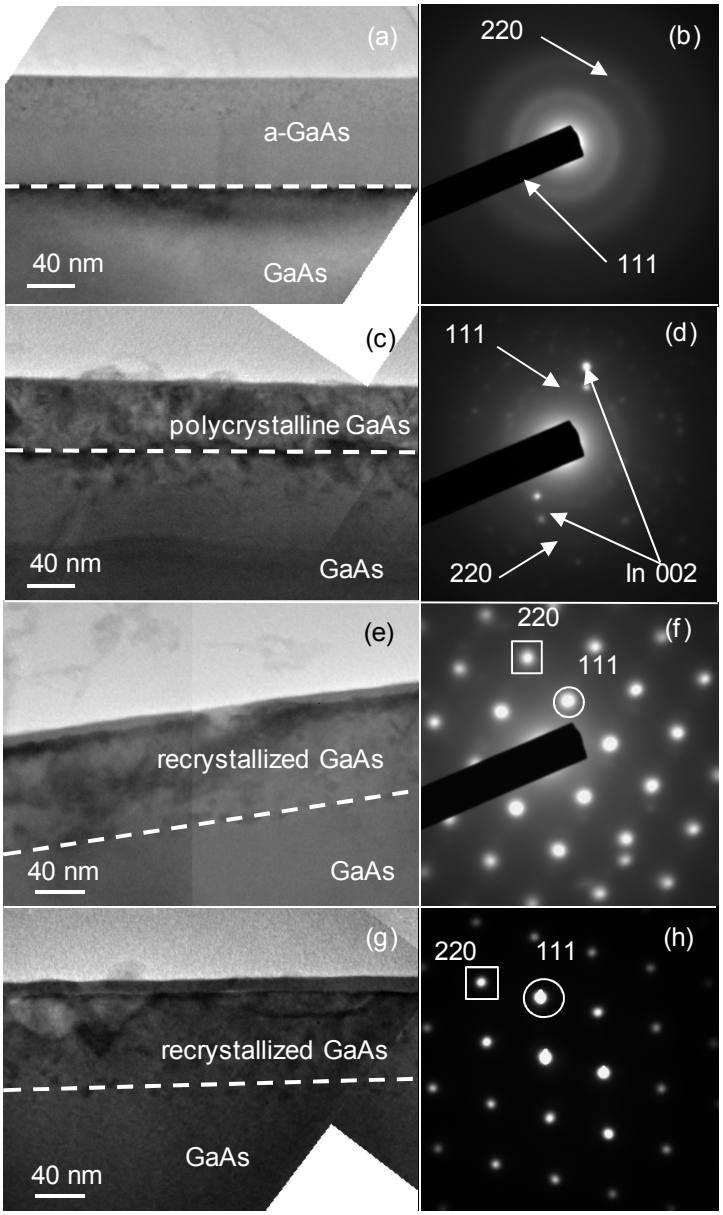

Fig. 3.5 Bright-field TEM images of (a) as-implanted, and following RTA at (c) low *T*, (e) medium *T*, and (g) high *T*. The corresponding SAD patterns, collected from the a-GaAs of (a) and the recrystallized layer of (c), (e), and (g), are presented in (b), (d), (f), and (h), respectively.

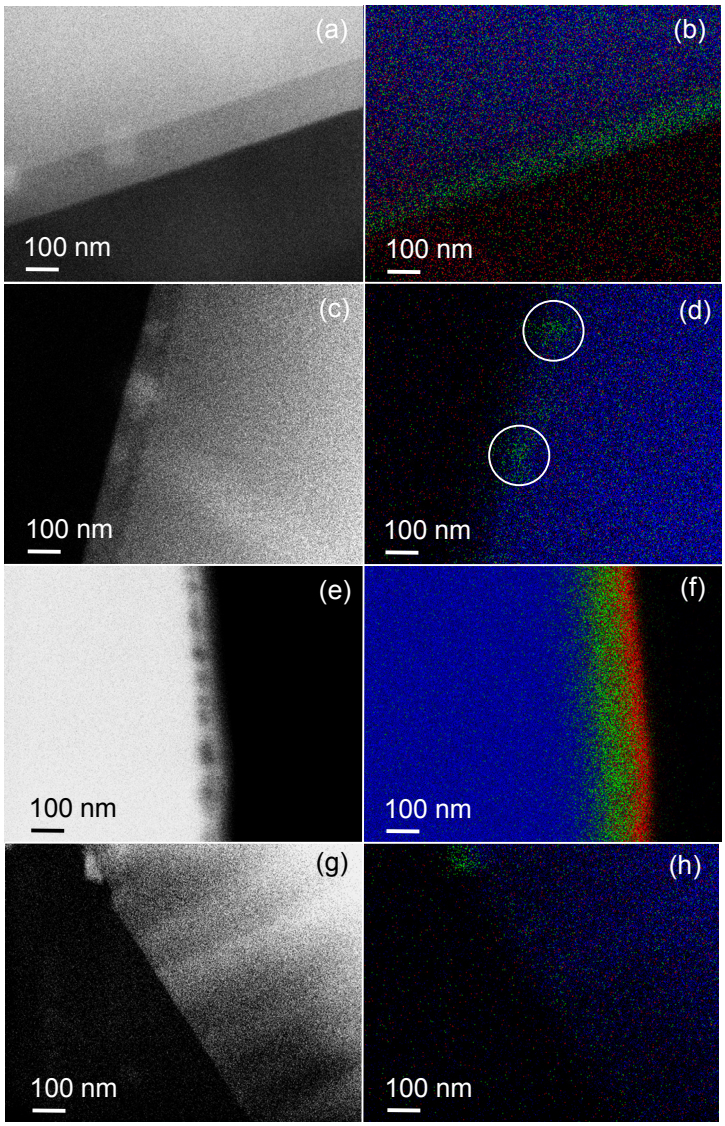

Fig. 3.6 Cross-sectional HAADF STEM images of (a) as-implanted, and following RTA at (c) low *T*, (e) medium *T*, and (g) high *T*. The corresponding composite elemental maps of Ga (blue), Al (red), and In (green) collected from (a), (c), (e), and (g), are presented in (b), (d), (f), and (h), respectively. The In NCs in (d) are circled as a guide to the eye.

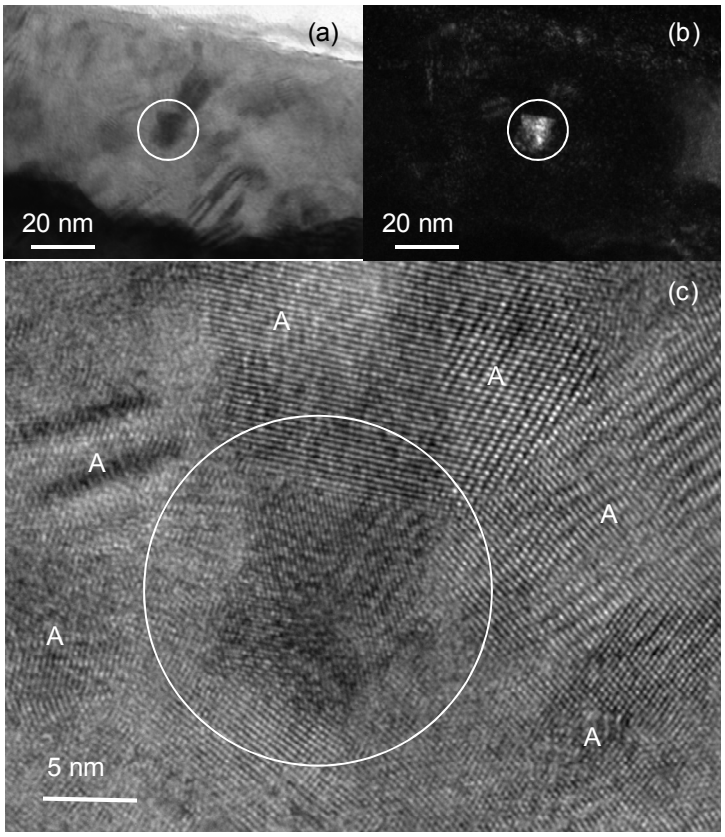

Fig. 3.7 Transmission electron microscopy (TEM) images of GaAs:In films following low *T* RTA: (a) bright-field, (b) In {110} dark-field, and (c) high-resolution. An opaque 13 nm diameter feature is shown in the bright-field image in (a). In the corresponding dark-field image (b), this feature appears bright, identifying it as an In NC. In (c), the high resolution TEM image of the same feature shows that the In NC is located at the boundary between GaAs crystallites, labeled "A". In (a)-(c), the In NC is circled as a guide to the eye.

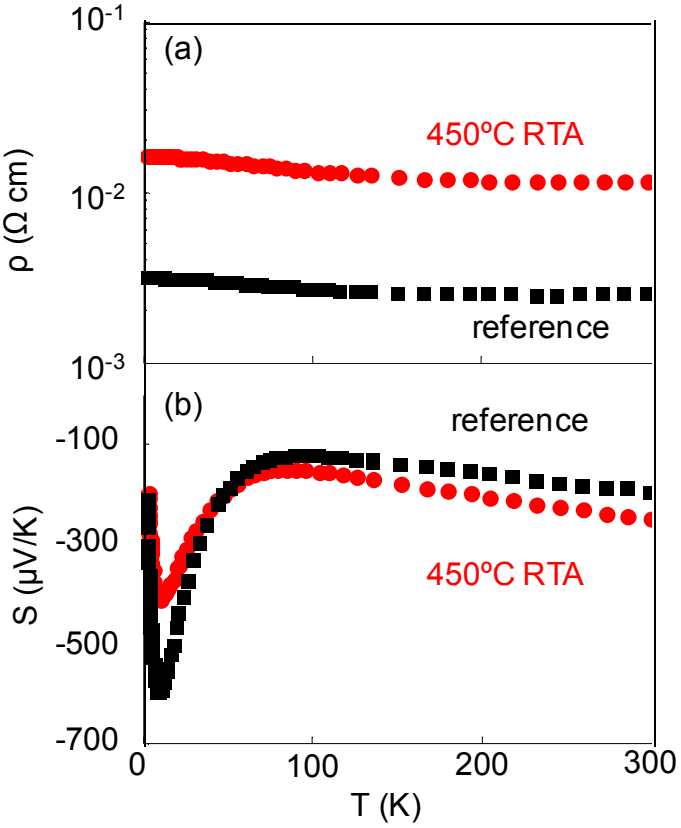

Fig. 3.8 (a) Resistivity, ρ, and (b) Seebeck coefficient, S, as a function of temperature for both the GaAs reference and the GaAs:In film low T RTA.

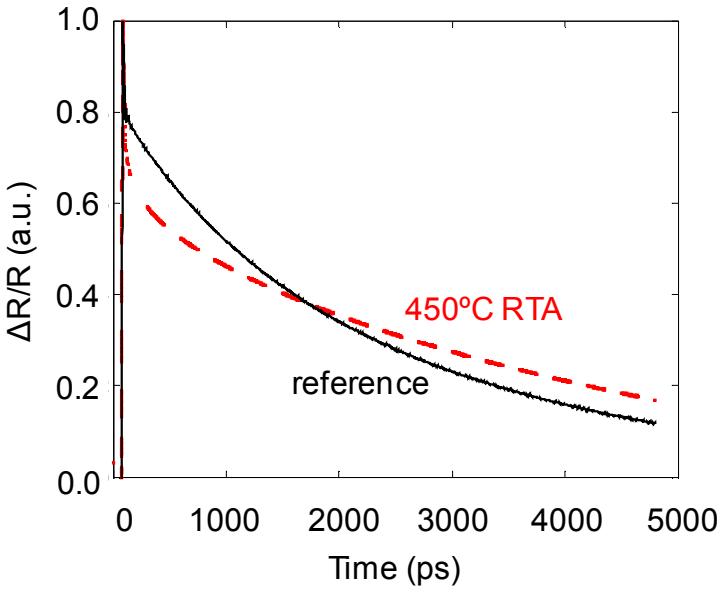

Fig. 3.9 Normalized transient reflectance as a function of time of the low *T* RTA film, in comparison to that of a GaAs reference.

3.6 References

[1] X. Weng, W. Ye, S. J. Clarke, R. S. Goldman, V. Rotberg, A. Daniel, and R. Clarke, *J. Appl. Phys*. **97**, 064301 (2005).

[2] X. Weng, S. J. Clarke, W. Ye, S. Kumar, R. S. Goldman, A. Daniel, R. Clarke, J. Holt, J. Sipowska, A. Francis, and V. Rotberg, *J. Appl. Phys.* **92**, 4012 (2002).

[3] L.D. Hicks, T.C. Harman, X. Sun, and M.S. Dresselhaus, Phys. Rev. B **53**, R10493 (1996).

[4] R. Venkatasubramanian, E. Siivola, T. Colpitts, and B. O'Quinn, Nature **413**, 597 (2001).

[5] M. Zebarjadi, G. Joshi, G. Zhu, B. Yu, A. Minnich, Y. Lan, X. Wang, M. Dresselhaus, Z. Ren, and G. Chen, Nano Lett. **11**, 2225 (2011).

[6] S.V. Faleev and F. Léonard, Phys. Rev. B **77**, 214304 (2008).

[7] A.W. Wood, R.R. Collino, P.T. Wang, Y.Q. Wang, and R.S. Goldman, Appl. Phys. Lett. **100**, 203113 (2012).

[8] M.V. Ardyshev and V.F. Pichugin, Russ. Phys. J. **47**, 175 (2004).

[9] J. Zuk, M.J. Clouter, M. Kulik, J. Romanek, and D. Maczka, Vacuum **58**, 543 (2000).

[10] S. Wei, L. Ferreira, and A. Zunger, Phys. Rev. B: Condens. Matter **41**, 8240 (1990).

[11] B. Lita, S. Ghaisas, R.S. Goldman, and M.R. Melloch, Appl. Phys. Lett. **75**, 4082 (1999).

[12] N. Mingo, Appl. Phys. Lett. **84**, 2652 (2004).

[13] S.S. Li and W.R. Thurder, Solid-State Electron. **20**, 609 (1977).

[14] R.M. Hill, Phys. Status Solidi **34** 601 (1976).

[15] S.M. Sze and J.C. Irvin, Solid State Electron. **11**, 599 (1968).

[16] R. Coates and E.W. Mitchell, J. Phys. C: Solid State Phys. **5**, L113 (1972).

[17] D. Rowe and K. Matsuura, in *CRC Handbook of Thermoelectrics* (CRC Press, Boca Raton, 1995).

[18] Due to the high resistivity of the high fluence film following RTA, Seebeck coefficient measurements were not possible.

[19] C. Herring, Phys. Rev. **96**, 1163 (1954).

[20] J.H. Wu, W. Ye, B.L. Cardozo, D. Saltzman, K. Sun, H. Sun, J.F. Mansfield, and R.S. Goldman, Appl. Phys. Lett. **95**, 153107 (2009).

[21] V.N. Brudnyi, M.A. Krivov, and A.I. Potapov, Solid State Commun. **34**, 117 (1980).

[22] F.G. Moore, P.B. Klein, and H.B. Dietrich, Nucl. Instrum. Methods Phys. Res. B **59-60**, 1103 (1991).

[23] F.G. Moore, P.B. Klein, and H.B. Dietrich, J. Appl. Phys. **72**, 2692 (1992).

[24] O.P. Sinha, T. Shripathi, N.P. Lalla, and P.C. Srivastava, Appl. Surf. Sci. **230**, 222 (2004).

[25] M.V. Warren, A.W. Wood, J.C. Canniff, F. Naab, C. Uher, and R.S. Goldman, Appl. Phys. Lett. **100**, 102101 (2012).

[26] J.M. Zide, D.O. Klenov, S. Stemmer, A.C. Gossard, G. Zeng, J.E. Bowers, D. Vashaee, and A. Shakouri, Appl. Phys. Lett. **87**, 112102 (2005).

[27] R.J. Stevens, A.N. Smith, and P.M. Norris, J. Heat Transfer **127**, 315 (2005).

[28] F. Cverna, *ASM Ready Reference: Thermal Properties of Metals* (ASM International, 2002), p. 341.

[29] P.E. Hopkins, J.C. Duda, S.P. Clark, C.P. Hains, T.J. Rotter, L.M. Phinney, and G. Balakrishnan, Appl. Phys. Lett. **98**, 161913 (2011).

[30] R.O. Carlson, G.A. Slack, and S.J. Silverman, J. Appl. Phys. **36**, 505 (1965).

Chapter 4

Influence of Embedded Bi Nanocrystals on GaAs Thermoelectric Properties

4.1 Overview

This chapter discusses our investigation into the ion beam synthesis of Bi NCs embedded in GaAs, as well as the influence of these NCs on the thermoelectric properties of the films. This chapter opens with background information on studies of Bi^+ implantation into GaAs and related materials. We then discuss the experimental methods used to characterize these GaAs:Bi films. Next, we discuss the influence of implantation and annealing on the microstructure of the films, and how this microstructure influences the GaAs thermoelectric properties. For all Bi^+ fluences, κ is reduced by ~30% in comparison to that of GaAs, presumably due to phonon scattering at Bi NC/GaAs matrix boundaries. The implantation process has also reduced both n and σ, with partial recovery following RTA. We then discuss the role of microstructure on the electrical and thermal conductivity of the GaAs:Bi films through a comparison with GaAs:In and GaAs:N films. This chapter concludes with a summary.

4.2 Background

Nanocomposite materials have been identified as promising candidates for high figure-of-merit thermoelectric materials. Due to the increased control of the density of states and hence, the energies of charge carriers, nanocomposite materials are predicted to have a significantly higher thermoelectric figure-of-merit ($Z = S^2\sigma/\kappa$, where S is the Seebeck coefficient, σ is the electrical conductivity, and κ is the thermal conductivity) in comparison to their bulk counterparts.[1] For example, enhancements of Z due to low dimensionality have been reported for Bi_2Te_3/Sb_2Te_3 superlattices[2] and embedded Si nanocrystals in SiGe.[3] Additionally, it has been suggested that embedded metallic nanoparticles enhance the Seebeck coefficient of a semiconducting matrix via electron energy filtering.[4] Recently, a variety of embedded nanocrystals have been synthesized by matrix-seeded growth, which involves ion-beam-amorphization of a semiconductor film, followed by nanoscale recrystallization via rapid thermal annealing (RTA).[5-10] For the case of In^+ implantation into GaAs, a sputter-mask method was developed to maximize the retained ion dose by limiting sputtering, yielding an ion-fluence dependent |S|, with an enormous Seebeck coefficient of -12 mV/K at 4 K for a fluence of 3.8×10^{17} cm^{-2}.[11] Furthermore, annealing at 450°C led to the formation of In nanocrystals (NCs), as well as an increase in the free carrier concentration and Seebeck coefficient while reducing the thermal conductivity by ~50%.[10] Due to the high atomic mass of Bi and its low, but finite, solubility in GaAs,[12] we consider GaAs:Bi for further reductions in thermal conductivity. Although low dose Bi^+ implantation at high (low) energies has been used to

produce damage tracks in GaAs:Bi[13] (electronic states in GaP and GaAs[14,15]), ion-beam synthesis of embedded Bi NCs in GaAs has not been explored.

4.3 Experiments

For these investigations, films were grown on semi-insulating (001) GaAs substrates using Ga, Al, As_2, and Si, as described elsewhere.[16] All samples consisted of an undoped GaAs buffer (250 nm thick), followed by Si-doped layers of GaAs (500 nm thick) and an AlAs sputter-mask (50 nm thick), all grown at 580 °C. The target free carrier concentration was $1x10^{18}$ cm^{-3}, within 50% of that predicted to maximize the GaAs power factor.[17] Following growth, a portion of the film was reserved as a reference sample, while the remainder was implanted, as described in Chapter 2, with 100 keV Bi^+, at fluences of $1.4x10^{16}$, $2.4x10^{16}$, and $5.6x10^{16}$ cm^{-2}, referred to as "low," "medium," and "high." At the low and medium (high) fluences, the AlAs layer is expected to be partially (fully) sputtered away.[11] To minimize channeling effects during implantation, a 7° angle of incidence with respect to the sample surface normal was utilized. During implantation, the substrate temperature was maintained at 77 K. Following implantation, RTA was performed in argon gas for 30 s at 450°C. During RTA, a GaAs proximity cap was used to minimize As out-diffusion.

Following growth and/or implantation and/or RTA, the temperature-dependence of the Seebeck coefficient $S(T)$ and room temperature carrier concentration (n), and conductivity (σ) were measured utilizing the methods detailed in Chapter 2. The thermal

conductivity of the films was measured using the time-domain thermoreflectance (TDTR) method described in Chapter 2. To examine the microstructure of the films, cross-sectional transmission electron microscopy (TEM), Energy Dispersive X-Ray Spectroscopy (EDX), and high-angle annular dark field (HAADF) scanning transmission electron microscopy (STEM) were performed, as described in Chapter 2.

4.4 Microstructural Evolution

Fig. 4.1 presents typical bright-field TEM images of as-implanted (a) low, (c) medium, and (e) high fluence films with corresponding SAD patterns as insets. For all three fluences, a ~90 nm amorphous surface layer is observed on top of single-crystal GaAs. However, for the medium fluence film, the amorphous surface layer is rippled with embedded GaAs crystallites near the surface. The SAD patterns of the low and high fluence films confirm the presence of an a-GaAs layer, while the SAD pattern of the medium fluence film exhibits an amorphous halo and diffraction spots, indicative of the presence of crystallites. To verify the presence and composition of these crystallites, the microstructure of the medium fluence film was further examined using bright- and dark-field TEM. In Fig. 4.2, close up views of the as-implanted medium fluence film are shown in the (a) bright-field and (b) dark-field images. The dark-field image in Fig. 4.2(b) was obtained using the GaAs {111} diffraction spot. A 40 nm feature is circled in Fig. 4.2(a) and Fig. 4.2(b). Since the feature appears bright in Fig. 4.2(b), it is attributed to a GaAs crystallite. For the high fluence film, voids are observed in the amorphous layer.

We now consider the influence of annealing on the microstructure of the GaAs:Bi films. Fig. 4.1(b), Fig. 4.1(d), and Fig. 4.1(f) present typical bright field TEM images, with corresponding SAD patterns as insets, of the annealed low, medium, and high fluence films, respectively. Following RTA, a ~85 nm surface layer (labeled "R") is observed on top of single-crystal GaAs, independent of ion fluence. The SAD patterns inset into Fig. 4.1(b), Fig. 4.1(d), and Fig. 4.1(f) show diffracted spots with d-spacings of 3.25 Å, within 1% of the {111} interplanar spacing of GaAs, indicative that the surface layers are recrystallized GaAs. Interestingly, these SAD patterns also include diffraction spots with d-spacings of 1.38 Å (Fig. 4.1(b)), 2.26 Å (Fig. 4.1(d)), and 2.36 Å (Fig. 4.1(f)), within 1% of the {018}, {110} and {104} interplanar spacing of Bi, respectively, implying the presence of Bi NCs embedded within single-crystal GaAs.

To confirm the presence of Bi NCs, HAADF imaging and EDX elemental mapping of the GaAs:Bi films was conducted. Fig. 4.3 presents typical HAADF images of post-RTA GaAs:Bi implanted at (a) low, (c) medium, and (e) high fluences. The corresponding EDX elemental maps are shown in Fig. 4.3(b), Fig. 4.3(d), and Fig. 4.3(f), with Bi and Ga atoms labeled in green and blue, respectively. EDX reveals the formation of ~80-150 nm Bi clusters (45-60 nm thick Bi-rich layers) for the low (medium and high) fluence film. The Bi clusters and Bi-rich regions are consistent with the Bi diffraction spots observed in Fig. 4.1(b), Fig. 4.1(d), and Fig. 4.1(f), indicating the presence of metallic Bi crystals.

4.5 Driving Forces of Bi and In NC Formation in GaAs

We now compare the influence of chemistry and electronic structure of In and Bi on the formation of metallic NCs and the microstructure of the GaAs films. Although Ga/In and As/Bi are isovalent and have similar electronegativities,[18] their covalent radii differ by up to 14 to 20%, respectively.[19] Thus, the solubility of In in GaAs is predicted to be much higher than that of Bi in GaAs.[20,12] While both the GaAs:In and GaAs:Bi films were subjected to similar implantation fluences and annealing conditions, their resulting microstructures differ. For the GaAs:In film, RTA at 450°C led to the nucleation of In NCs within a polycrystalline GaAs matrix. However, for the GaAs:Bi films, RTA at the same temperature led to Bi NC nucleation within a single-crystal GaAs matrix. This difference in recrystallization of the GaAs is presumably due to the presence of Bi, which has been shown to act as a surfactant during epitaxial growth of both stoichiometric and As-rich GaAs.[21] We hypothesize that the surfactant effect of Bi allows the GaAs film to recrystallize as a single crystal, similar to solid-phase epitaxy of Si films on sapphire substrates.[22]

4.6 Influence of Bi NCs on the Seebeck Coefficient

To examine the influence of the Bi NCs on the Seebeck effect in GaAs:Bi, we consider the *T*-dependence of *S* of the implanted plus annealed films, in comparison with those of the GaAs reference, as shown in Fig. 4.4. At the lowest measurement

temperatures, shown in the inset to Fig. 4.4, both the Bi NC-containing and reference GaAs films exhibit a rapid increase of $|S|$ up to a peak at ~10 K, similar to earlier reports of GaAs:In.[11] For $T > 10$ K, $|S|$ rapidly decreases with increasing temperature to ~100 K. This T-dependence of S is a manifestation of a strong electron-phonon interaction, referred to as the phonon-drag effect. For the low and medium fluence GaAs:Bi films, the maximum values of $|S|$ are 35 and 100 μV/K higher than that of the GaAs reference, presumably due to free carrier trapping at implantation-induced defects. On the other hand, for the high fluence GaAs:Bi film, the maximum value of $|S|$ is reduced by 24 μV/K in comparison to that of the GaAs reference, presumably due to *enhanced* phonon scattering at vacancies.[23] Indeed, in the high fluence GaAs:Bi film, RTA has led to atomic diffusion into voids, resulting in void collapse as shown in Fig. 4.1(f), which likely leads to an increased concentration of vacancy point defects. For $T > 100$ K, the so-called diffusion regime, where electron diffusion is driven by the temperature gradient, $|S|$ increases monotonically with T, for all films, independent of implantation dose. Thus, Bi NCs have a negligible influence on $|S|$ of GaAs, similar to the negligible effect of In NCs reported earlier.[10] Thus, it is evident that increases in $|S|$ are primarily due to decreases in n, rather than any density of states modifications due to the presence of Bi or In NCs.

4.7 Influence of Microstructure on Electrical Properties

We now consider the influence of microstructure on the relationship between free carrier concentration, n, and electrical conductivity, σ, of the GaAs:Bi films in

comparison with those of GaAs:In[10] and GaAs:N,[24] as shown in Fig. 4.5(a). In the plot of σ vs. n, dashed lines form an "envelope" corresponding to a mobility range of 1000 to 4000 $cm^2\ V^{-1}s^{-1}$. It is interesting to note that all GaAs-based films lie within this envelope, independent of implantation species. The GaAs film mobilities are typically near the upper end of the range (4000 $cm^2\ V^{-1}s^{-1}$), while the GaAs:Bi, GaAs:In, and GaAs:N mobilities range from near the lower end (1000 $cm^2\ V^{-1}s^{-1}$) to the mid-range of the envelope, depending on their microstructure. For example, the mobilities of the as-implanted GaAs:Bi, GaAs:In, and GaAs:N films, which consist of amorphous layers, lie near the lower end of the range. Similarly, the mobility of the GaAs:In film following RTA, with a polycrystalline microstructure, lies near the lower end of this range. Meanwhile, the mobilities of the GaAs:Bi films following RTA, which have recrystallized, lie near the mid-range of the envelope. The trends for n are similar. Following implantation with Bi, In, or N, n is reduced in comparison to that of pristine GaAs films, presumably due to an increase in the concentration of implantation-induced point defects which trap carriers.[25] It is interesting to note that the n of the as-implanted GaAs:Bi film with crystalline remnants is higher than that of the other GaAs:Bi films, consistent with the increase in active dopant concentration expected in crystalline versus amorphous GaAs.[26] Following RTA, both n and σ of the implanted GaAs films increase, most likely due to the annealing out of defects that trap carriers. For the In NC-containing film, n is doubled following RTA, due to the In NC acting as electron donors, similar to that reported for ErAs particles embedded in GaAs.[27] Since the Fermi level of In is within the room temperature thermal energy, k_BT, of the conduction band edge of GaAs, the In NCs act as electron donors.[28] Unlike the In NCs, the separation between the GaAs

conduction band edge and the Bi NC Fermi energy exceeds k_BT by ~0.1 eV; thus, the Bi NCs do not act as electron donors.

4.8 Influence of Microstructure on Thermal Properties

We have examined the relationship between microstructure and the thermal conductivity, κ, of the films, using an analysis of TDTR measurements, as described in Ref. 10. Fig. 4.5(b) shows κ as a function of n for the GaAs:Bi films after RTA, in comparison with those of GaAs reference films.[29] For GaAs, since κ is weakly dependent on n, we consider $\kappa_{total} \approx \kappa_{lattice}$,[29] shown as the nearly horizontal dashed line in the plot in Fig. 4.5(b). For all GaAs films, κ is similar to the reported values of $\kappa_{lattice}$. For both GaAs:In and GaAs:Bi, κ is decreased in comparison to that of pristine GaAs, presumably due to phonon scattering at NC boundaries. The GaAs:In film exhibits the lowest κ of the NC-containing films, most likely due to its polycrystalline structure which would scatter more phonons than the single crystal structure of the GaAs:Bi films.

4.9 Conclusions

In summary, we examined the influence of embedded Bi NCs on n, σ, S, and κ of GaAs prepared by ion implantation followed by RTA. Following implantation, the microstructure consists of a-GaAs with or without crystalline remnants, voids, and/or ripples. Following RTA, all layers have transformed to single crystal GaAs with

embedded Bi NCs. The Bi NC-containing films exhibit a ~30% reduction in κ, due to phonon scattering at NC boundaries. The implantation process leads to the formation of carrier-trapping defects, reducing both n and σ; RTA anneals out a portion of these defects, leading to a partial recovery of n and σ. Furthermore, the Bi NCs have a negligible influence on the room temperature Seebeck coefficient. By comparing the role of microstructure on the electrical and thermal conductivity of the GaAs:Bi, GaAs:In, and GaAs:N films, we have demonstrated a general trend of n and σ reduction following ion-implantation, while RTA yields a partial recovery of n and σ, as well as a reduction in κ due to phonon scattering.

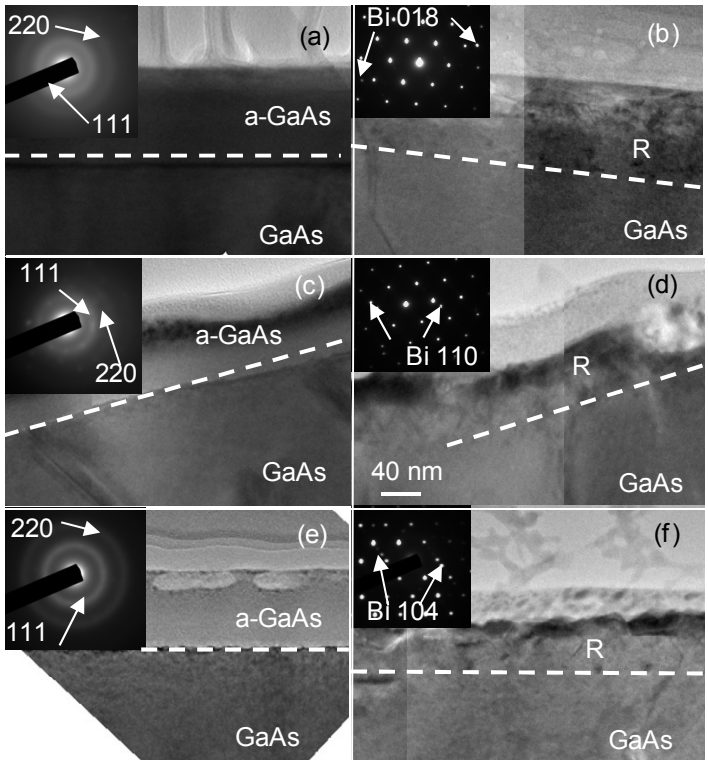

Fig. 4.1 Bright-field TEM images of low (a and b), medium (c and d), and high (e and f) ion fluence films both as-implanted and after RTA, respectively. The insets in (a)-(f) are the corresponding SAD patterns. All images share the scale used in (d).

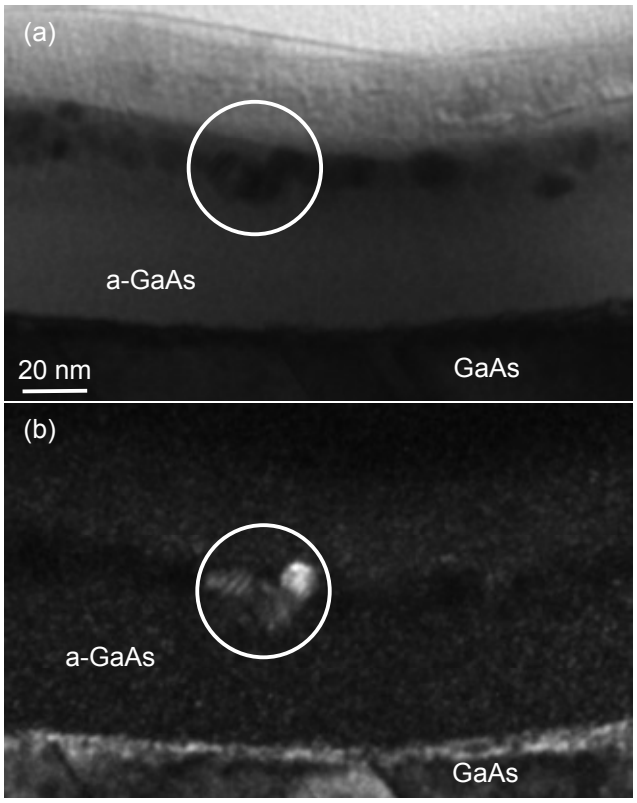

Fig. 4.2 TEM images of the medium fluence film following implantation: (a) bright-field, and (b) GaAs {111} dark-field. An opaque feature is shown in the bright-field image (a). In the corresponding dark-field image (b), this feature appears bright, identifying it as a GaAs crystallite.

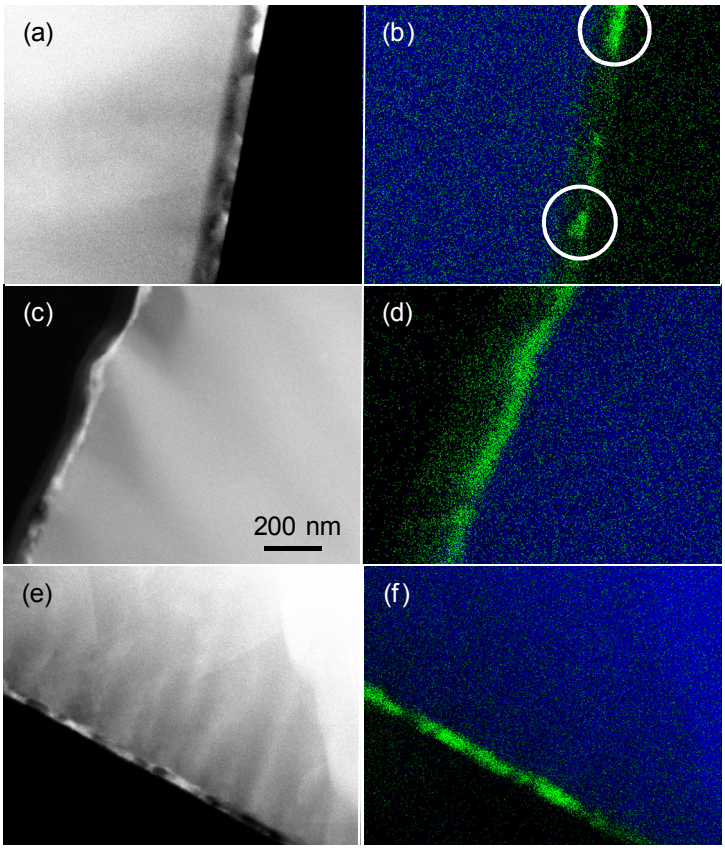

Fig. 4.3 Cross-sectional HAADF STEM images of GaAs:Bi films implanted at (a) low, (c) medium, and (e) high ion fluence following RTA. The corresponding composite elemental maps of Ga (blue) and Bi (green) collected from (a), (c), and (e) are presented in (b), (d), and (f), respectively. The Bi NCs in (b) are circled as a guide to the eye. All images share the scale used in (c).

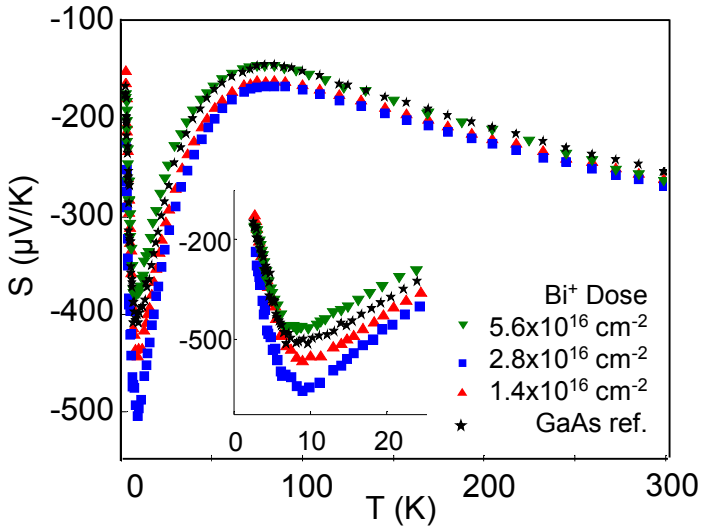

Fig. 4.4 Seebeck coefficient, *S*, as a function of temperature for the low *T* RTA film in comparison to that of the reference film. Inset is a detailed view of the phonon drag peak, indicating similar peak positions for all films.

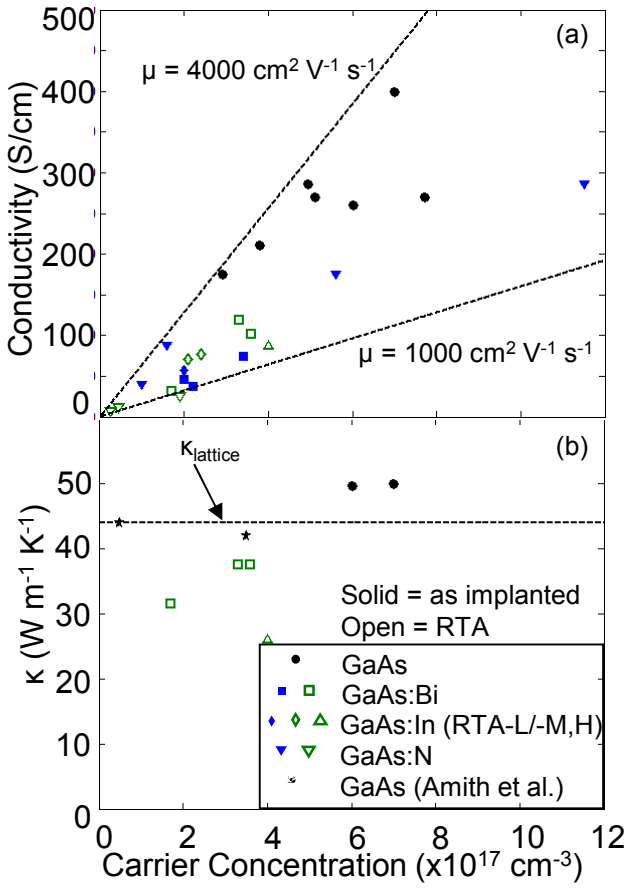

Fig. 4.5 (a) electrical conductivity, σ, and (c) thermal conductivity, κ, as a function of free carrier concentration, *n*. The black data points corresponds to GaAs films, while the solid blue and open green data points correspond to the as implanted and RTA films, respectively. The conductivity of all films fall within an "envelope" of mobility ranging from 1000 to 4000 $cm^2\ V^{-1}\ s^{-1}$, with pristine GaAs falling near the higher end of the range and as-implanted GaAs near the lower end of the range. The mobilities of the implanted GaAs films falls in the mid-range of the envelope, dependent on the microstructure of the film.

4.10 References

[1] L.D. Hicks, T.C. Harman, X. Sun, and M.S. Dresselhaus, Phys. Rev. B **53**, R10493 (1996).

[2] R. Venkatasubramanian, E. Siivola, T. Colpitts, and B. O'Quinn, Nature **413**, 597 (2001).

[3] M. Zebarjadi, G. Joshi, G. Zhu, B. Yu, A. Minnich, Y. Lan, X. Wang, M. Dresselhaus, Z. Ren, and G. Chen, Nano Lett. **11**, 2225 (2011).

[4] S.V. Faleev and F. Léonard, Phys. Rev. B **77**, 214304 (2008).

[5] X. Weng, W. Ye, S.J. Clarke, R.S. Goldman, V. Rotberg, A. Daniel, and R. Clarke, J. Appl. Phys. **97**, 064301 (2005).

[6] A.W. Wood, R.R. Collino, P.T. Wang, Y.Q. Wang, and R.S. Goldman, Appl. Phys. Lett. **100**, 203113 (2012).

[7] J.C. Canniff, A.W. Wood, and R.S. Goldman, Appl. Phys. Lett. **102**, (2013).

[8] A.W. Wood, R.R. Collino, B.L. Cardozo, F. Naab, Y.Q. Wang, and R.S. Goldman, J. Appl. Phys. **110**, 124307 (2011).

[9] A.W. Wood, X. Weng, Y.Q. Wang, and R.S. Goldman, Appl. Phys. Lett. **99**, 093108 (2011).

[10] M.V. Warren, J.C. Canniff, H. Chi, E. Morag, F. Naab, V.A. Stoica, R. Clarke, C. Uher, and R.S. Goldman, J. Appl. Phys. **114**, 043704 (2013).

[11] M.V. Warren, A.W. Wood, J.C. Canniff, F. Naab, C. Uher, and R.S. Goldman, Appl. Phys. Lett. **100**, 102101 (2012).

[12] S.B. Eugenev and N.B. Ganina, Izv. Akad. Nauk SSSR, Neorg. Mater. **20**, 561 (1984).

[13] F. Komarov, L. Vlasukova, V. Yuvchenko, T. Petlitzkaya, and P. Zukowski, VACUUM **78**, 353 (2005).

[14] J.L. Merz, L.C. Feldman, and E.A. Sadowski, Radiat. Eff. **6**, 285 (1970).

[15] M.J. Seong and A. Mascarenhas, (private communication).

[16] B. Lita, S. Ghaisas, R.S. Goldman, and M.R. Melloch, Appl. Phys. Lett. **75**, 4082 (1999).

[17] N. Mingo, Appl. Phys. Lett. **84**, 2652 (2004).

[18] W.D. Callister, *Materials Science and Engineering: An Introduction, 8th Edition*, 6th ed. (Wiley, Hoboken, 2003), p 19.

[19] J.C. Slater, J. Chem. Phys. **41**, 3199 (1964).

[20] S. Wei, L. Ferreira, and A. Zunger, Phys. Rev. B **41**, 8240 (1990).

[21] S. Tixier, M. Adamcyk, E.C. Young, J.H. Schmid, and T. Tiedje, J. Cryst. Growth **251**, 449 (2003).

[22] Q.-Y. Wang, J.-P. Nie, F. Yu, Z.-L. Liu, and Y.-H. Yu, Mater. Sci. Eng. B **72**, 189 (2000).

[23] G.J. Snyder and E.S. Toberer, Nat Mater **7**, 105 (2008).

[24] R.R. Collino, Ph.D. Thesis, University of Michigan, 2010.

[25] R. Coates and E.W. Mitchell, J. Phys. PART C SOLID STATE Phys. **5**, L113 (1972).

[26] W.G. Opyd, J.F. Gibbons, and A.J. Mardinly, Appl. Phys. Lett. **53**, 1515 (1988).

[27] J.M. Zide, D.O. Klenov, S. Stemmer, A.C. Gossard, G. Zeng, J.E. Bowers, D. Vashaee, and A. Shakouri, Appl. Phys. Lett. **87**, 112102 (2005).

[28] H.B. Michaelson, J. Appl. Phys. **48**, 4729 (1977).

[29] A. Amith, I. Kudman, and E.F. Steigmeier, Phys Rev **138**, A1270 (1965).

Chapter 5

Summary and Suggestions for Future Work

5.1 Summary

In this thesis, the formation of embedded metallic In and Bi nanocrystals (NCs) and their influence on the thermoelectric properties of GaAs were investigated. We examined the roles of In^+ fluence and annealing temperature on the nucleation of In NCs, and the influence of these NCs on the free carrier concentration, n, Seebeck coefficient, S, and the electrical resistivity, ρ, and thermal, κ, conductivity of the GaAs film. We also studied the influence of Bi^+ fluence on the formation of embedded Bi NCs and the effects of these NCs on the thermoelectric properties of GaAs. This thesis reveals new insights into the structure-property relationship of ion-implanted GaAs. Embedded metallic NCs show promise for thermoelectric applications via κ reduction. Based on these results, it is suggested that epitaxial growth of embedded NCs will result in a reduction in κ while simultaneously preserving σ.

In Chapter 3, we examined the formation of metallic In NCs embedded within GaAs, via studies of the roles of ion fluence and annealing temperature. The low and medium fluence films consist of a residual AlAs layer on a-GaAs, indicative that the medium fluence is optimal for saturating the GaAs with In atoms. Unlike the low and

medium fluence films, the high fluence film exhibits no remaining AlAs, consisting of an a-GaAs layer with crystalline remnants. RTA leads to the formation of a recrystallized GaAs layer with stacking faults likely due to simultaneous recrystallization from the AlAs and crystalline GaAs interfaces in the low and medium fluence films, while a polycrystalline film is formed in the high fluence film. Both S and ρ increase with ion fluence, with the high fluence film exhibiting both electrons ($T < 10$ K) and holes ($T > 10$ K) as charge carriers with corresponding phonon drag peaks of -12 mV/K at 4 K and +2 mV/K at 15 K. For the low and medium (high) fluence films before and after RTA, $\ln(\rho)$ is independent (dependent) on $T^{-1/4}$, indicative of extended-band (variable-range-hopping) conduction. With the optimal In^+ fluence determined, we studied the influence of annealing temperature on the formation and thermoelectric properties of In NCs. Annealing at the lowest temperature (450ºC) leads to the nucleation of In NCs. These In NCs enhance the free carrier concentration, while electron and phonon scattering at crystallite boundaries increases the resistivity and reduces the thermal conductivity. Furthermore, the room temperature Seebeck coefficient exhibits a 25% increase due to carrier trapping.

In Chapter 4, we studied the influence of Bi^+ ion fluence on the formation of Bi NCs embedded in GaAs and their influence on the GaAs thermoelectric properties. Following implantation, the microstructure consists of a-GaAs with or without crystalline remnants, voids, and/or ripples. Following RTA, all layers have transformed to single crystal GaAs with embedded Bi NCs. The Bi NC-containing films exhibit a ~30% reduction in κ, due to phonon scattering at NC boundaries. The implantation process leads to the formation of carrier-trapping defects, reducing both n and σ; RTA anneals out

a portion of these defects, leading to a partial recovery of n and σ. Furthermore, the Bi NCs have a negligible influence on the room temperature Seebeck coefficient. By comparing the role of microstructure on the electrical and thermal conductivity of the GaAs:Bi, GaAs:In, and GaAs:N films, we have demonstrated a general trend of n and σ reduction following ion-implantation, while RTA yields a partial recovery of n and σ, as well as a reduction in κ due to phonon scattering.

5.2 Suggestions for Future Work

In Chapters 3 and 4, we presented a method for the formation of embedded In and Bi NCs and their influence on the thermoelectric properties of GaAs. However, due to the implantation/dopant profiles of the films, the thermoelectric properties of a combination of the NC-containing layer and the doped GaAs layer underneath were measured simultaneously. Since the measured thermoelectric properties were a convolution of multiple layers, the values of the thermoelectric properties are not accurate. The metallic NCs were formed via ion implantation followed by rapid thermal annealing at 450ºC. Implantation-induced defects serve to lower n, thereby lowering σ, and increasing S. Indium NCs act as electron donors, somewhat increasing n, while both Bi and In NCs scatter phonons, reducing κ. However, in both cases, the increase in S and reduction in κ do not compensate for the reduction in σ caused during ion implantation. If these metallic NC/GaAs nanocomposites are to exhibit an enhanced figure-of-merit in comparison to GaAs, the reduction in σ, and therefore the concentration of implantation-induced defects,

must be minimized. In the following sections, we will discuss a method for measuring the electrical properties of the nanostructured layer, allowing a more accurate measurement of the thermoelectric properties of the NC-containing films. We will then describe three suggestions for future work that are expected to allow the fabrication metallic nanocrystals embedded in GaAs with minimal reductions in σ. First, we will discuss annealing GaAs:Bi films at temperatures higher than 450°C and/or times longer than 30 s. We will then discuss utilizing a Bi focused ion beam to locally fabricate embedded Bi NCs. Finally, we will suggest a method for fabricating embedded metallic NCs in GaAs utilizing epitaxial growth.

5.2.1 Measuring the Electrical Properties of Multi-layer Films

One method for extracting the electrical transport properties of a single layer within a multi-layer structure is the mobility spectrum analysis.[1] In this analysis, Hall effect measurements in a Hall bar geometry are performed over a range of magnetic fields, B, up to $B > \mu^{-1}$. The parallel and transverse conductivities (σ_{xx} and σ_{xy}, respectively) are measured as a function of magnetic field and are a sum of the contribution from each conducting channel:[2]

$$\sigma_{xx}(B_j) = \sum_{i=1}^{N} \frac{[s^p(\mu_i) + s^n(\mu_i)]\Delta\mu_i}{1 + \mu_i^2 B_j^2} \tag{5.1}$$

$$\sigma_{xy}(B_j) = \sum_{i=1}^{N} \frac{[s^p(\mu_i) - s^n(\mu_i)]\mu_i B_j \Delta\mu_i}{1 + \mu_i^2 B_j^2} \tag{5.2}$$

where s^p and s^n are hole and electron conductivity density functions, respectively, and $\Delta\mu = \mu_i - \mu_{i-1}$. Thus, we generate a system of equations, allowing us to measure the carrier concentration and electrical conductivity of only the NC-containing layers in the implanted and annealed GaAs films, allowing an accurate reporting of the figure-of-merit of GaAs with embedded metallic nanocrystals.

5.2.2 Influence of Annealing Temperature and Time on GaAs:Bi Thermoelectric Properties

As discussed in Chapter 4, ion-beam synthesis of embedded Bi NCs results in a reduction in κ and a negligible increase in S, but a marked decrease in σ. This decrease in σ is due to implantation-induced defects which both reduce n and scatter electrons. For a GaAs:Bi nanocomposite to achieve a figure-of-merit ($ZT=S^2T\sigma/\kappa$) larger than that of bulk GaAs, the reduction in σ, and therefore the concentration of implantation-induced defects, must be minimized. One method of minimizing these implantation-induced defects is by annealing at higher temperatures. It has been shown for Zn^+ implanted GaAs that as annealing temperature increases, the residual damage in the GaAs films decreases, reaching a constant minimum damage concentration for anneals at and above 700°C.[3] Furthermore, annealing the Zn^+ implanted films at temperatures higher than 400°C leads to an increase in σ, with a maximum σ achieved for anneals at 900°C. In Chapter 4, it was demonstrated that annealing GaAs:In films at temperatures higher than 450°C leads to the formation of a uniform InGaAs layer, however this is not expected to be the case for

GaAs:Bi for two reasons. Firstly, the large atomic radius of Bi makes the probability of its occupying an As site unlikely. Secondly, as evidenced in the Bi-GaAs phase diagram, the solubility of Bi in GaAs is very low.[4] These properties of Bi indicate that annealing of GaAs:Bi at temperatures between 700 and 900°C should result in an increased σ, while still nucleating Bi NCs which will scatter phonons, reducing κ, resulting in an overall increase in ZT.

Another method for minimizing the concentration of implantation-induced defects is annealing the GaAs:Bi films for longer times. For low-temperature grown GaAs, it has been shown that as annealing time increases, the concentration of defects within the film decreases.[5] Thus, longer annealing times for the GaAs:Bi films should lead to a reduction in the concentration of n- and σ-reducing defects. However, due to the low solubility of Bi in GaAs, Bi NC nucleation is still likely, resulting in an enhancement in the scattering of phonons and therefore a reduction in κ.

5.2.3 Localized Bi NC Formation via Focused Bi Ion Beams

Another method for minimizing the implantation-induced reduction in n and σ is to utilize a focused ion beam (FIB) to localize the implantation-induced damage in the GaAs films. It has recently been shown that N^+ implantation into GaAs followed by annealing leads to the formation of GaN NCs.[6] However, localized irradiation of the GaAs films with a Ga^+ FIB prior to annealing, leads to the preferential nucleation of GaN NCs in the regions affected by the FIB.[7] Since NC nucleation occurs in regions of highest

damage to the GaAs lattice, this localized formation of NCs, termed "directed matrix seeding", is attributed to the additional ion-induced damage caused by the FIB. We propose using a Bi^+ FIB to locally implant Bi into GaAs, followed by RTA to nucleate Bi NCs. By utilizing an FIB, it is possible to implant Bi in a much smaller area, limited by the ion beam spot size. Following RTA, Bi NCs are expected to nucleate within the areas implanted by the Bi^+ FIB. Since, a majority of the GaAs film will be unaffected by implantation-induced defects, presumably resulting in a less drastic reduction in n and σ, and therefore an overall increase in ZT in comparison to GaAs.

5.2.4 Epitaxial Growth of GaAs with Embedded Bi Nanocrystals

A third method for minimizing the reduction in σ, and therefore the concentration of implantation-induced defects, is to fabricate these embedded NCs without the use of ion implantation. Recently, there has been interest in the fabrication of semiconductor nanocomposites with embedded metallic and semimetallic nanoparticles via epitaxial growth. That work has focused on the fabrication of embedded ErAs or TbAs nanoparticles in GaAs and its derivative alloys InGaAs and InGaAlAs.[8-12] For these films, the Seebeck coefficient is less than that of the GaAs:Bi films. However, n and σ are both larger than those of the GaAs:Bi films, while κ is less than that of the GaAs:Bi films. These results indicate that epitaxial grown embedded nanocrystals in GaAs-based materials leads to an overall increase in ZT, presumably due to the much higher σ of the epitaxially grown films. It has been demonstrated that deposition of Bi on GaAs surfaces

during epitaxial growth leads to the nucleation of Bi islands.[13] It is likely that alternating deposition of GaAs and Bi layers will lead to the formation of a GaAs:Bi nanocomposite. Although this nanocomposite may contain electron-scattering defects formed during growth, the concentration of defects is expected to be much lower than in nanocomposites formed via ion-beam synthesis, which will likely lead to a higher σ, and therefore a higher ZT.

5.3 References

[1] I. Vurgaftman, J.R. Meyer, C.A. Hoffman, D. Redfern, J. Antoszewski, L. Faraone, and J.R. Lindemuth, J. Appl. Phys. **84**, 4966 (1998).

[2] J.R. Meyer, C.A. Hoffman, J. Antoszewski, and L. Faraone, J. Appl. Phys. **81**, 709 (1997).

[3] S.S. Kular, B.J. Sealy, K.G. Stephens, D. Sadana, and G.R. Booker, Solid-State Electron. **23**, 831 (1980).

[4] S.B. Eugenev, and N.B. Ganina, Izv. Akad. Nauk SSSR, Neorg. Mater., **20**, 561 (1984).

[5] D.E. Bliss, W. Walukiewicz, J.W. Ager, E.E. Haller, K.T. Chan, and S. Tanigawa, J. Appl. Phys. **71**, 1699 (1992).

[6] A.W. Wood, R.R. Collino, P.T. Wang, Y.Q. Wang, and R.S. Goldman, Appl. Phys. Lett. 100, 203113 (2012).

[7] A.W. Wood, R.R. Collino, B.L. Cardozo, F. Naab, Y.Q. Wang, and R.S. Goldman, J. Appl. Phys. 110, 124307 (2011).

[8] J.M. Zide, D.O. Klenov, S. Stemmer, A.C. Gossard, G. Zeng, J.E. Bowers, D. Vashaee, and A. Shakouri, Appl. Phys. Lett. **87**, 112102 (2005).

[9] J.M.O. Zide, J.-H. Bahk, R. Singh, M. Zebarjadi, G. Zeng, H. Lu, J.P. Feser, D. Xu, S.L. Singer, Z.X. Bian, A. Majumdar, J.E. Bowers, A. Shakouri, and A.C. Gossard, J. Appl. Phys. **108**, 123702 (2010).

[10] L.E. Cassels, T.E. Buehl, P.G. Burke, C.J.P. m, A.C. Gossard, G. Pernot, A. Shakouri, C.R. Haughn, M.F. Doty, and J.M.O. Zide, J Vac Sci Technol B **29**, 03C114 (2011).

[11] L.E. Clinger, G. Pernot, T.E. Buehl, P.G. Burke, A.C. Gossard, C.J.P. m, A. Shakouri, and J.M.O. Zide, J. Appl. Phys. **111**, 094312 (2012).

[12] E. Selezneva, L.E. Clinger, A.T. Ramu, G. Pernot, T.E. Buehl, T. Favaloro, J.-H. Bahk, Z. Bian, J.E. Bowers, J.M.O. Zide, and A. Shakouri, J. Electron. Mater. **41**, 1820 (2012).

[13] G. Vardar, S.W. Paleg, M.V. Warren, M. Kang, S. Jeon, and R.S. Goldman, Appl. Phys. Lett. **102**, 042106 (2013).

Appendices

Appendix A

Selected Area Electron Diffraction

When electrons impinge on atomic planes (with interplanar spacing d) at a glancing angle of θ, the Bragg equation is satisfied:[1,2]

$$2d\sin\theta = \lambda \tag{A.1}$$

where λ is the wavelength of the electrons. It is shown in Fig. A.1 that the angle between the incident electron beam and the diffracted electron beam is 2θ. If the electron beam is incident on a polycrystalline rather than singe crystal specimen, the electron beams will be diffracted into a cone with semi-angle 2θ, shown in Fig. A.2. The electron beams are then incident on the TEM phosphor screen, forming a circle of radius R, such that

$$R/L = \tan 2\theta \tag{A.2}$$

where L is the distance between the specimen and the phosphor screen. For electrons with energy on the order of tens of keV, the angle 2θ is only a few degrees.[1] Thus, the small angle approximation that $\sin\theta \approx \theta$ or $\tan 2\theta \approx \theta$ is applicable, allowing us to solve Eqs. A.1 and A.2 for θ and set them equal to each other, finding

$$Rd = \lambda L \tag{A.3}$$

where λ and L are constants associated with the TEM. We then measure R, allowing us to solve for d. These measurements of R are described below.

The diffraction image is imported into a graphics program capable of denoting pixel coordinates, such as Microsoft Paint. For single crystal diffraction spots, pixel coordinates for spot pairs on opposite sides of the transmitted beam are denoted. For polycrystalline samples, several pixel coordinates from each ring are denoted for points on the ring, making sure to denote pixel coordinates from points along the entire circumference ring when possible.

The pixel coordinates denoted are then converted to a radius by finding the center of the diffraction pattern. The method utilized for finding the center of the pattern is dependent on whether the diffraction pattern contains single crystal diffraction spots or polycrystalline rings. When the image consists of single crystal diffraction spots, the center is found by connecting multiple paired diffraction spots along a line, as shown in Fig. A.3(a). The intersection of these lines corresponds to the center of the diffraction pattern and the pixel coordinates are noted. When the diffraction pattern consists of only polycrystalline rings, the center of the image may be found by drawing a rectangle within the outermost ring, as shown in Fig. A.3(b). The diagonals of the rectangle intersect at the center of the diffraction pattern and the pixel coordinates are denoted.

The pixel coordinates from spot n either from a single crystal diffraction spot or along the polycrystalline ring (x_n,y_n) are then normalized with respect to the coordinates of the center of the diffraction pattern (x_c,y_c) using the following relation:

$$(x_{norm}, y_{norm}) = (x_n - x_c, y_n - y_c). \tag{A.4}$$

The radius, in units of pixels, are calculated using the following equation:

$$R = \sqrt{x_{norm}^2 + y_{norm}^2}\ . \tag{A.5}$$

To obtain d from the radii calculated from Eq. A.5, a known value of d must be used. When an image contains single crystal diffraction spots, d is obtained directly from standard values listed with the International Centre for Diffraction Data (ICDD). When the diffraction pattern consists only of polycrystalline rings, R and its associated d (related by Eq. A.3) can be obtained from a single crystal diffraction pattern taken during the same TEM session using an identical camera length and accelerating voltage. This is because the right side of Eq. A.3 is microscope-specific constant, allowing two arbitrary reflections in the diffraction pattern to be related by the equation

$$R_1 d_1 = R_2 d_2 = \lambda L \tag{A.6}$$

where d_1 and R_1 are the known interplanar spacing and radius of the diffracted spots, respectively. We then solve for the unknown interplanar spacing d_2:

$$d_2 = \frac{R_1 d_1}{R_2} \tag{A.7}$$

The source of the diffracted spot (e.g. GaAs, In, or Bi) is then determined by comparing the calculated d spacings with the d spacings from ICDD.

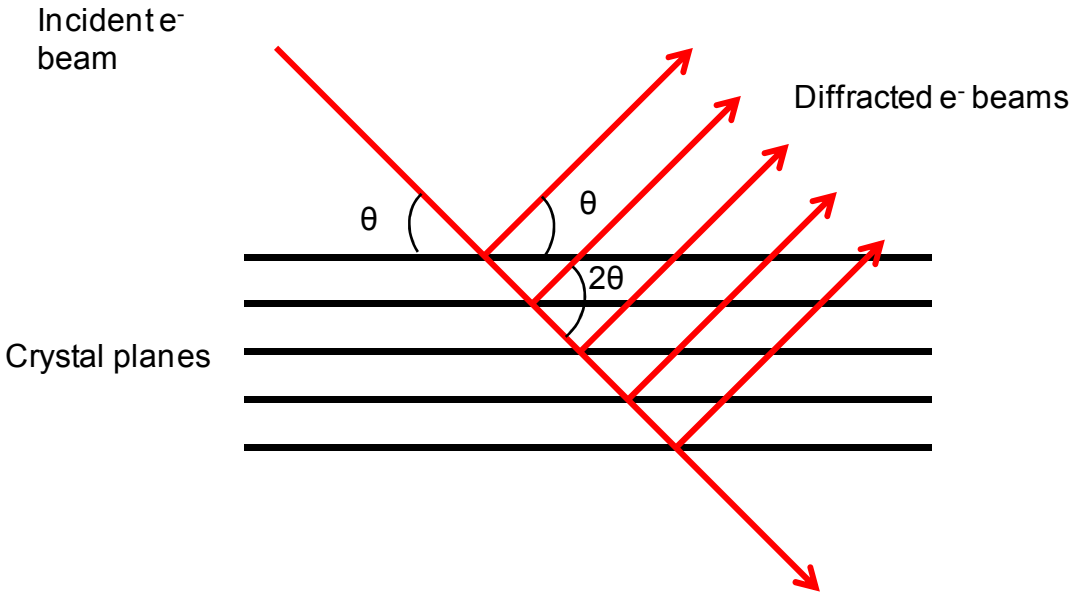

Fig. A.1 Schematic of electron diffraction at crystal planes. The electron beam is incident upon the sample at angle θ. The electron beams are then diffracted at an angle 2 θ with respect to the incident beam. (Adapted from Ref. 1)

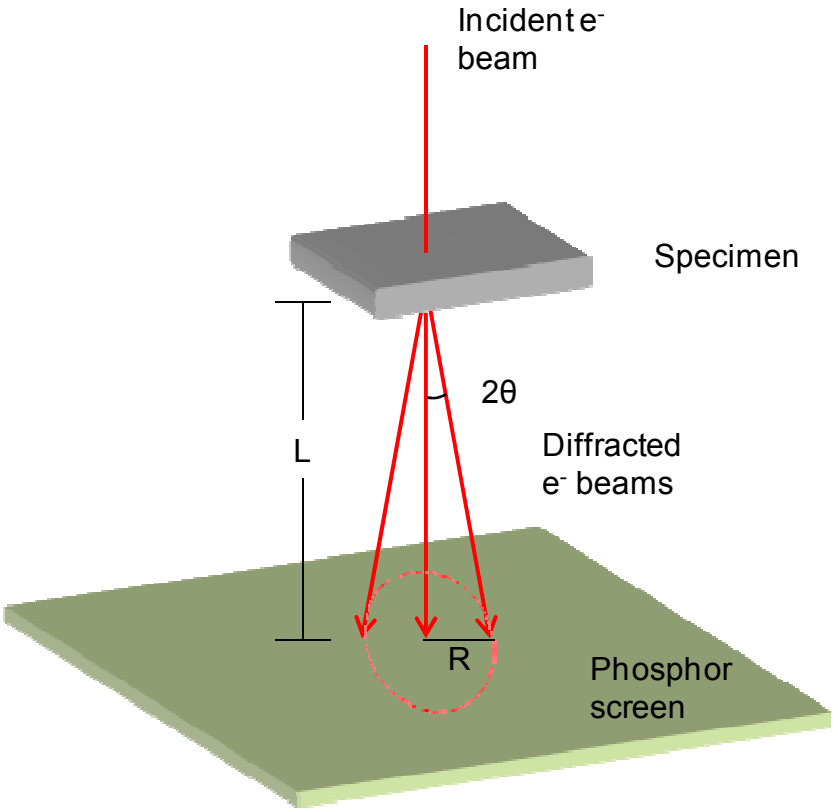

Fig. A.2 Schematic representation of electron diffraction from a polycrystalline sample. The sample diffracts the incident electron beam into a cone with semi-angle 2θ. These diffracted beams form a circle of radius R on the phosphor imaging screen. (Adapted from Ref. 1)

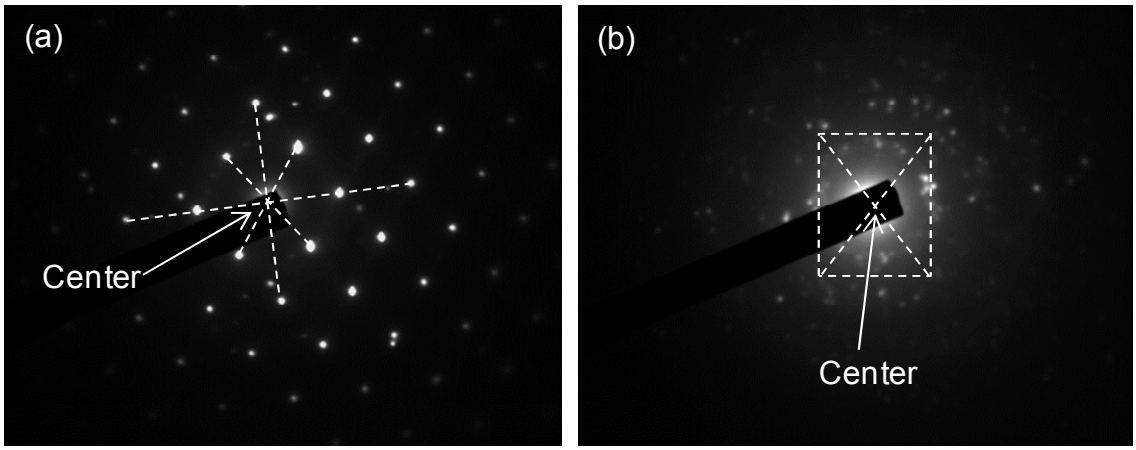

Fig. A.3 Examples of the methods used to determine the center of a diffraction pattern for a (a) single-crystal and (b) polycrystalline pattern.

References

[1] T. B Rymer, *Electron Diffraction* (Methuen & Co. Ltd., London 1970) p.7.

[2] D. B. Williams and C. Barry Carter, eds. *Transmission Electron Microscopy* (Springer Science+Business Media, Inc. New York, 1996), Chapter 35.

Appendix B

Sputter-Mask for the Enhancement of Retained Ion Concentration

To maximize the retained In concentration by preventing In sputtering, we utilized a 50 nm AlAs "sputter mask". The AlAs layer thickness and In^+ dose were selected based upon the Profile Code[1] simulations shown in Fig. B.1. For this purpose, we approximated the sputter yield of AlAs (Y^{AlAs}) for our 100 keV In^+ ions with the measured Y^{AlAs} for 30 keV Ga^+ ions.[2] Since 100 keV ions are expected to be decelerated via electronic stopping to 30 keV,[3] this is a reasonable approximation. We further corrected the Y^{AlAs} value for the mass of In as follows:

$$Y_{In} = \frac{M_{In}}{M_{Ga}} Y_{Ga} \tag{B.1}$$

where Y_{In} (Y_{Ga}) is the sputter yield for In (Ga) ions, and M_{In} (M_{Ga}) is the atomic mass of In (Ga). With this correction, Y_{In} for 30 keV In^+ ions implanted into AlAs is similar to that of Y_{In} for 30 keV In^+ ions implanted into SiO_2, based upon SRIM[4] simulations. Therefore, we performed Profile Code[1] simulations of the implantation of 30 keV In^+ into a SiO_2/GaAs structure. The parameters used in these simulations are tabulated in Appendix D. Figure B.1 shows depth vs. In concentration for various In^+ fluences overlayed on a schematic SiO_2/GaAs heterostructure, as well as the steady-state In concentration for In^+ implanted GaAs without a masking layer. As the implantation dose

increases, the SiO_2 layer is sputtered away, while the retained In concentration in the GaAs layer increases. The highest retained In concentration is predicted when the SiO_2 layer is nearly sputtered away. For comparison, the steady state In depth vs. concentration profile is plotted as well. The Profile Code simulations predict a maximum In concentration with (without) the sputter mask is $9x10^{21}$ cm^{-3} ($5x10^{20}$ cm^{-3}). Therefore, we used $3.8x10^{15}$ – $3.8x10^{17}$ cm^{-2} In^{+} fluences with a 50 nm thick AlAs masking layer.

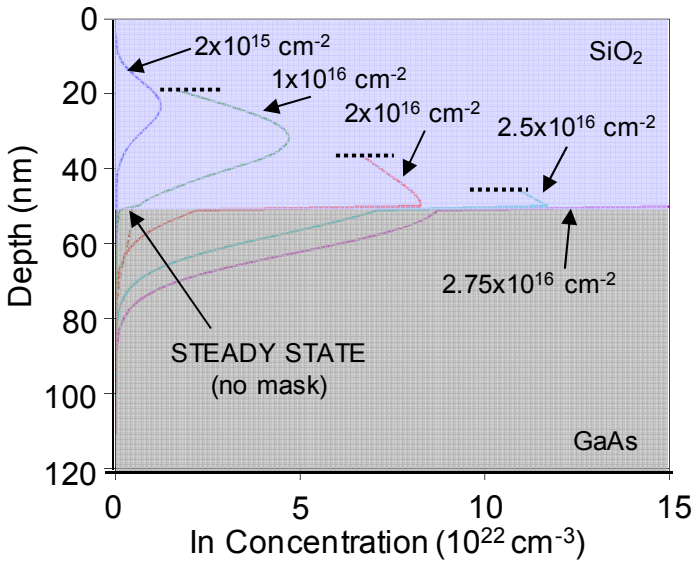

Fig. B.1 Profile Code simulations of depth vs. In concentration for various In^+ fluences overlayed on a schematic SiO_2/GaAs heterostructure, as well as the steady state depth vs In concentration profile, with a maximum [In] of $5x10^{20}$ cm^{-3} for GaAs without a sputter mask. The depth of complete sputtering of the SiO_2 mask is indicated by the dashed line (s) at the beginning of the curves labeled $1x10^{16}$, $2x10^{16}$, and $2.5x10^{16}$ cm^{-2}. For an ion fluence of $2.75x10^{16}$ cm^{-2}, nearly all of the SiO_2 is sputtered away, with a peak [In] in the GaAs layer of $9x10^{21}$ cm^{-3}.

References

[1] *Profile Code* (Implant Sciences Corp., Wakefield, MA, 1992).

[2] K.A. Grossklaus and J.M. Millunchick, J. Appl. Phys. **109**, 014319 (2011).

[3] J.R. Tesmer and M.A. Nastasi, editors, *Handbook of Modern Ion Beam Materials Analysis* (Materials Research Society, Pittsburgh, Pa., 1995).

[4] J.F. Ziegler, J.P. Biersack, and U. Littmark, *The Stopping and Range of Ions in Matter* (Pergamon, New York, 1985).

Appendix C

Time-domain Thermoreflectance Measurements of Thermal Conductivity

Time-domain thermoreflectance measurements utilize a pump/probe experimental setup shown schematically in Fig. C.. A short laser pulse (<1 psec) with energy Q is incident on a metal film with thickness d. We assume that the optical absorption length, ξ, is much smaller than d and that the area illuminated by the light pulse, A, is large in comparison to d and ξ. Thus, the total energy deposited per unit volume at a distance z into the film is given by

$$\Delta T(z) = (1-R)\frac{Q}{C(\xi A)}\exp^{-z/\xi} \tag{C.1}$$

where R is the reflectivity.[1]

To extract the thermal conductivity, κ, of the sample, we compare ΔT to the results of a one-dimensional heat flow calculation, as described in Ref. 2. The heat flow calculation is facilitated by assuming that the temperature of the metal film is uniform throughout its thickness at times greater than 30 ps and that the lateral heat flow is negligible compared to the heat flow into the sample. With these assumptions, the heat flow away from the metal/sample interface will obey the one-dimensional diffusion equation:

$$\kappa\frac{\partial^2 T_s(z,t)}{\partial z^2} = c_s\frac{\partial T_s(z,t)}{\partial t} \tag{C.2}$$

where $T_s(z,t)$ is the temperature of the sample at depth z and time t, and c_s is the specific heat per unit volume of the sample.

The rate of energy flux into the sample must also be equal to the energy loss from the metal film:

$$\kappa \left. \frac{\partial T_s(z,t)}{\partial z} \right|_{z=0} = c_s d \frac{\partial T_m(t)}{\partial t} \tag{C.3}$$

where $T_m(t)$ is the temperature of the metal film.

We then consider the effect of the thermal-boundary resistance, R_K, which is defined as the ratio of the temperature difference across the metal/sample interface to the areal heat flow through the metal/sample interface. This is described by:

$$\kappa \left. \frac{\partial T_s(z,t)}{\partial z} \right|_{z=0} = -\frac{T_m(t) - T_s(0,t)}{R_K} \tag{C.4}$$

We then vary κ and R_K until we have obtained a curve that best fits the data. An example of a well-fit curve to experimental data is shown in Fig. C.2.

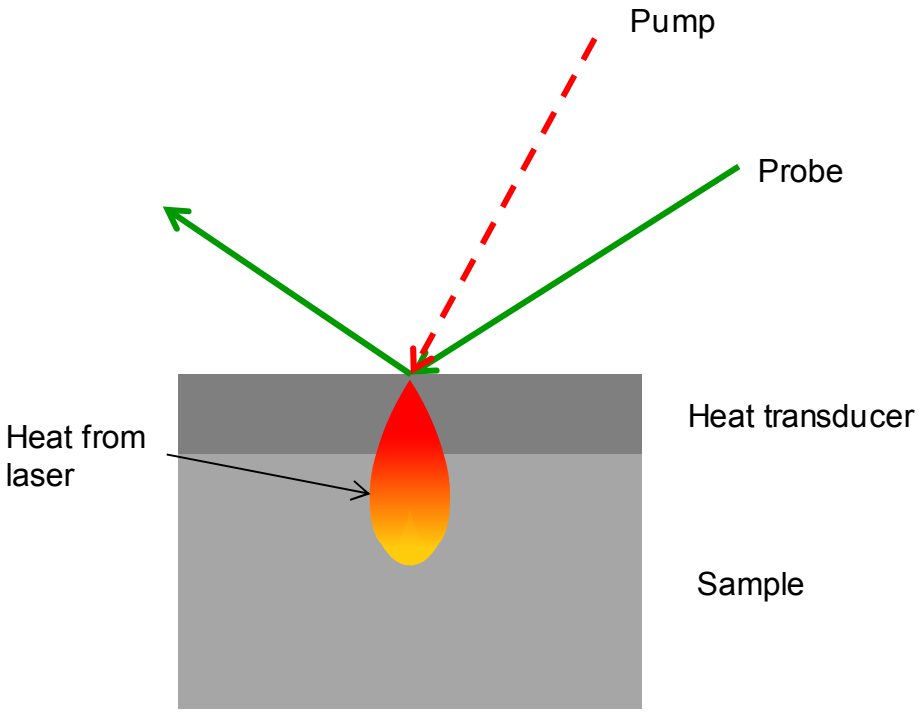

Fig. C.1 Schematic representation for time-domain thermoreflectance measurements. A pump laser pulse incident on a metal heat transducer film heats the film. The heat then flows into the sample. A probe laser pulse is used to detect changes in the reflectance.

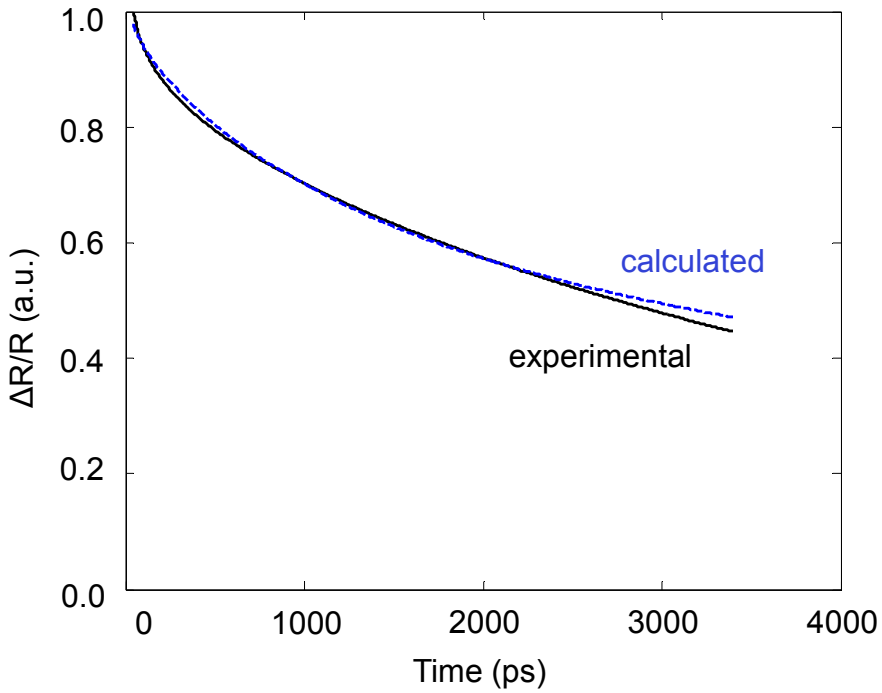

Fig. C.2 Example of a calculated thermoreflectance curve (dashed blue line) that is in good agreement with experimentally measured (solid black line) thermoreflectance data.

References

[1] C. Thomsen, H. T. Grahn, H. J. Maris, and J. Tauc, *Phys. Rev. B* **34**, 4129 (1986).

[2] G. A. Antonelli, B. Perrin, B. C. Daly, and D. C. Cahill, *MRS Bulletin* **31**, 607 (2006).

Appendix D

Simulation Parameters

In this Appendix, the parameters used in simulations for this work are tabulated. For the sputter mask calculations detailed in Appendix B, the simulation parameters are tabulated in Table D.1. For the thermal conductivity calculations detailed in Appendix C, the parameters are tabulated in Table D.2.

Table D.1 Simulation Parameters used in sputter mask calculations

SRIM Simulation Parameters	
Ion Species	indium
Ion Mass	114.9 amu
Ion Energy	30 keV
Ion Angle of Incidence	7°
Target Material	SiO_2
Target Atomic Mass	15.99 amu (O); 28.08 amu (Si)
Target Density	2.32 g/cm^3
Target Thickness	1000 nm
Profile Code Simulation Parameters	
Ion Species	indium
Ion Mass	115 amu
Ion Energy	30 keV
Ion Angle of Incidence	7°
Ion Dose	$2x10^{15} – 2.75x10^{16}$ cm^{-2}
Sputter Mask Material	SiO_2
Sputter Mask Density	2.27 g/cm^3
Sputter Mask Thickness	500 nm
Target Material	GaAs
Target Density	5.31 g/cm^3
Target Thickness	infinite

Table D.2 Parameters used in thermal conductivity calculations

Transducer Heat Capacity	2.43 J K^{-1} cm^{-3} (from Ref. 1)
Film Heat Capacity	1.76 J K^{-1} cm^{-3} (from Ref. 2)

References

[1] R.H. Schumm, D.D. Wagman, S. Bailey, W.H. Evans, and V.B. Parker in National Bureau of Standards (USA, 1973) Technical Notes 270-1 to 270-8.

[2] A.S. Jordan, J. Cryst. Growth, **49**, 631 (1980).

Appendix E

Tabulated Data

In this Appendix, data from various measurements are tabulated. In Table E.3, the results of TEM, Hall measurement, and Seebeck coefficient studies of In^+-implanted GaAs films are tabulated. In Table E.4, we list the results of similar studies for Bi^+-implanted GaAs films.

Table E.3 Summary of Hall, Seebeck, and TEM measurements of GaAs:In samples

Sample Name	Sample Processing	σ (S/cm) Room Temp.	n (cm^{-3})	S (μV/K)		TEM Results
				Room Temp.	Phonon Drag	
Samples used in Ch. 3.3: Effect of In^+ Fluence						
759	Reference sample	230	$5x10^{17}$	-234	-800	N/A
751-1538	Fluence = $3.8x10^{15}$ cm^{-2}	16.5	$1x10^{17}$	-321	-1088	68 nm a-GaAs
751-1638	Fluence = $3.8x10^{16}$ cm^{-2}	9.2	$4x10^{16}$	-339	-1096	143 nm a-GaAs
751-1738	Fluence = $3.8x10^{17}$ cm^{-2}	0.21	Too low to measure	+290	-11200 (e^-) +1704 (h^+)	104 nm a-GaAs + crystal remnant
751-1538-600	Fluence = $3.8x10^{15}$ cm^{-2} + 600°C RTA	76.8	$2x10^{17}$	-309	-1016	100 nm recrystallized GaAs
751-1638-600	Fluence = $3.8x10^{16}$ cm^{-2} + 600°C RTA	57.6	$1x10^{17}$	-300	-1000	126 nm recrystallized GaAs
751-1738-600	Fluence = $3.8x10^{17}$ cm^{-2} + 600°C RTA	0.18	Too resistive to measure			Poly-recrystallized GaAs
Samples used in Ch. 3.4: Effect of RTA Temperature						
818	Reference sample	400	$7.0x10^{17}$	-200	-600	N/A
818-1638	Fluence = $3.8x10^{16}$ cm^{-2}	57.1	$2.0x10^{17}$	N/A	N/A	100 nm a-GaAs
818-1638-450	Fluence = $3.8x10^{16}$ cm^{-2} + 450°C RTA	87.0	$4.0x10^{17}$	-251	-409	63 nm poly-GaAs + In NC
818-1638-500	Fluence = $3.8x10^{16}$ cm^{-2} + 500°C RTA	76.9	$2.4x10^{17}$	N/A	N/A	96 nm recrystallized GaAs
818-1638-550	Fluence = $3.8x10^{16}$ cm^{-2} + 550°C RTA	71.4	$2.1x10^{17}$	N/A	N/A	89 nm recrystallized GaAs

Table E.4 Summary of Hall, Seebeck, and TEM measurements of GaAs:Bi samples

Sample Name	Sample Processing	σ (S/cm) Room Temp.	n (cm^{-3})	S (μV/K)		TEM Results
				Room Temp.	Phonon Drag	
854	Reference sample	260	$6.0x10^{17}$	-253	-400	N/A
854-1614	Fluence = $1.4x10^{16}$ cm^{-2}	46	$2.0x10^{17}$	N/A	N/A	103 nm a-GaAs
854-1628	Fluence = $2.8x10^{16}$ cm^{-2}	75	$3.4x10^{17}$	N/A	N/A	78.7 nm a-GaAs + ripples
854-1656	Fluence = $5.6x10^{16}$ cm^{-2}	37	$2.2x10^{17}$	N/A	N/A	88.8 ± 1.9 nm a-GaAs + voids
854-1614-450	Fluence = $1.4x10^{16}$ cm^{-2} + 450°C RTA	119	$3.3x10^{17}$	-261	-436	92.4 nm recrystallized GaAs + Bi NC
854-1628-450	Fluence = $2.8x10^{16}$ cm^{-2} + 450°C RTA	101	$3.6x10^{17}$	-268	-497	80 nm recrystallized GaAs + Bi NC
854-1656-450	Fluence = $5.6x10^{16}$ cm^{-2} + 450°C RTA	32	$1.7x10^{17}$	-262	-376	84.7 nm recrystallized GaAs + Bi NC